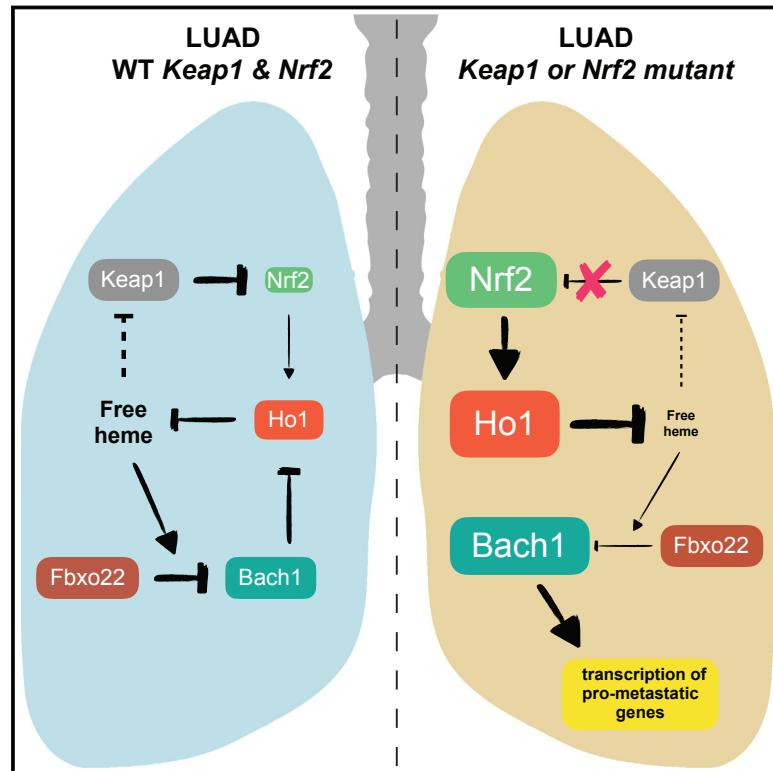


Nrf2 Activation Promotes Lung Cancer Metastasis by Inhibiting the Degradation of Bach1

Graphical Abstract



Authors

Luca Lignitto, Sarah E. LeBoeuf, Harrison Homer, ..., Thales Papagiannakopoulos, Michele Pagano

Correspondence

papagt01@nyumc.org (T.P.), michele.pagano@nyumc.org (M.P.)

In Brief

Stabilization of the transcription factor Bach1 drives metastasis of lung adenocarcinoma and this can be counteracted by the pharmacological inhibition of heme oxygenase.

Highlights

- Keap1 loss and Nrf2 activation induce metastasis in LUAD by accumulating Bach1
- Nrf2 inhibits the Fbxo22-mediated degradation of Bach1 in a Ho1-dependent manner
- Bach1 signature is associated with metastasis and shortened survival in LUAD patients
- Ho1 inhibitors reduce LUAD metastasis in a Fbxo22- and Bach1-dependent manner



Nrf2 Activation Promotes Lung Cancer Metastasis by Inhibiting the Degradation of Bach1

Luca Lignitto,^{1,2} Sarah E. LeBoeuf,^{2,3} Harrison Homer,^{1,2} Shaowen Jiang,^{1,2} Manor Askenazi,^{1,4} Triantafyllia R. Karakousi,^{2,3} Harvey I. Pass,^{2,5} Arjun J. Bhutkar,⁶ Aristotelis Tsigirgos,^{2,3} Beatrix Ueberheide,^{1,2} Volkan I. Sayin,^{2,3} Thales Papagiannakopoulos,^{2,3,*} and Michele Pagano^{1,2,7,8,*}

¹Department of Biochemistry and Molecular Pharmacology, New York University School of Medicine, New York, NY 10016, USA

²Perlmutter NYU Cancer Center, New York University School of Medicine, New York, NY 10016, USA

³Department of Pathology, New York University School of Medicine, New York, NY 10016, USA

⁴Biomedical Hosting LLC, 33 Lewis Avenue, Arlington, MA 02474, USA

⁵Department of Cardiothoracic Surgery, New York University School of Medicine, New York, NY 10016, USA

⁶Koch Institute for Integrative Cancer Research, MIT, 77 Massachusetts Ave. Building 76, Cambridge, MA 02139, USA

⁷Howard Hughes Medical Institute, New York University School of Medicine, New York, NY 10016, USA

⁸Lead Contact

*Correspondence: papagt01@nyumc.org (T.P.), michele.pagano@nyumc.org (M.P.)

<https://doi.org/10.1016/j.cell.2019.06.003>

SUMMARY

Approximately 30% of human lung cancers acquire mutations in either *Keap1* or *Nfe2l2*, resulting in the stabilization of Nrf2, the *Nfe2l2* gene product, which controls oxidative homeostasis. Here, we show that heme triggers the degradation of Bach1, a pro-metastatic transcription factor, by promoting its interaction with the ubiquitin ligase Fbxo22. Nrf2 accumulation in lung cancers causes the stabilization of Bach1 by inducing Ho1, the enzyme catabolizing heme. In mouse models of lung cancers, loss of *Keap1* or *Fbxo22* induces metastasis in a Bach1-dependent manner. Pharmacological inhibition of Ho1 suppresses metastasis in a Fbxo22-dependent manner. Human metastatic lung cancer display high levels of Ho1 and Bach1. Bach1 transcriptional signature is associated with poor survival and metastasis in lung cancer patients. We propose that Nrf2 activates a metastatic program by inhibiting the heme- and Fbxo22-mediated degradation of Bach1, and that Ho1 inhibitors represent an effective therapeutic strategy to prevent lung cancer metastasis.

INTRODUCTION

Lung cancer is the leading cause of cancer-related death in the United States and worldwide (Bar et al., 2008). During lung tumorigenesis, cancer cells enhance their metabolic output, which, in turn, increases the production of reactive oxygen species (ROS). To maintain oxidative homeostasis, ~30% of non-small-cell lung cancer (NSCLCs) increase the transcription of antioxidant genes by acquiring either stabilizing mutations in *Nfe2l2* (encoding Nrf2, the master transcriptional regulator of the cells antioxidant program) or by selecting for inactivating mutations in its negative regulator, *Keap1* (Cancer Genome Atlas Research Network, 2014). *Keap1* is a substrate receptor of a Cul3-RING

ubiquitin ligase (CRL3) that, in physiological conditions, constitutively binds and targets Nrf2 for degradation (Rojo de la Vega et al., 2018). In response to oxidative stress, the Keap1-Nrf2 binding is inhibited and, consequently, Nrf2 is stabilized.

Metastasis is a major contributor to the mortality of cancer patients. Lung adenocarcinoma (LUAD), a NSCLC subtype, is a highly metastatic disease with approximately 22% of patients displaying local lymph node metastases and 57% distant metastases at the time of diagnosis (Brady et al., 2016; Caswell et al., 2014; Chuang et al., 2017). *Keap1* mutations are associated with advanced stage IV metastatic disease and poor prognosis (Romero et al., 2017), suggesting a possible role for *Keap1* loss role in the metastatic cascade.

The transcriptional regulator Bach1 (BTB domain and CNC homolog 1) functions as a molecular sensor of intracellular heme, tuning transcription to the fluctuation of heme levels (Ogawa et al., 2001; Sun et al., 2002). Heme plays a role in various biological reactions by interacting with many inactive apo-proteins to generate functional hemoproteins (Mense and Zhang, 2006). Most forms of oxidative stress elicit heme release from hemoproteins, leading to more oxidative stress as free heme catalyzes a massive production of free radicals (Gozzelino et al., 2010; Pamplona et al., 2007). Cells avoid the self-amplifying, pro-oxidant effects of free heme through a variety of mechanisms, particularly, via the rapid induction of heme oxygenase-1 (Ho1), which catabolizes free heme (Li and Stocker, 2009).

Bach1, together with Nrf2 and the Maf transcription factors, controls the expression of Ho1 and other antioxidant genes (Oyake et al., 1996; Sun et al., 2004). Bach1 dimerizes with Mafs to repress Maf-recognition elements. In response to oxidative stress, Nrf2 accumulates through Keap1 inactivation, and increased levels of free heme promotes the proteasome-dependent degradation of Bach1 (Zenke-Kawasaki et al., 2007). Nrf2, then, dimerizes with Mafs and induces the transcriptional activation of antioxidant target genes, including *Ho1* (Tebay et al., 2015). Notably, in addition to its role in the Maf-Nrf2 pathway, Bach1 promotes invasion and metastasis by activating the transcription of critical metastatic genes (Lee et al., 2013; Liang et al., 2012; Yun et al., 2011).



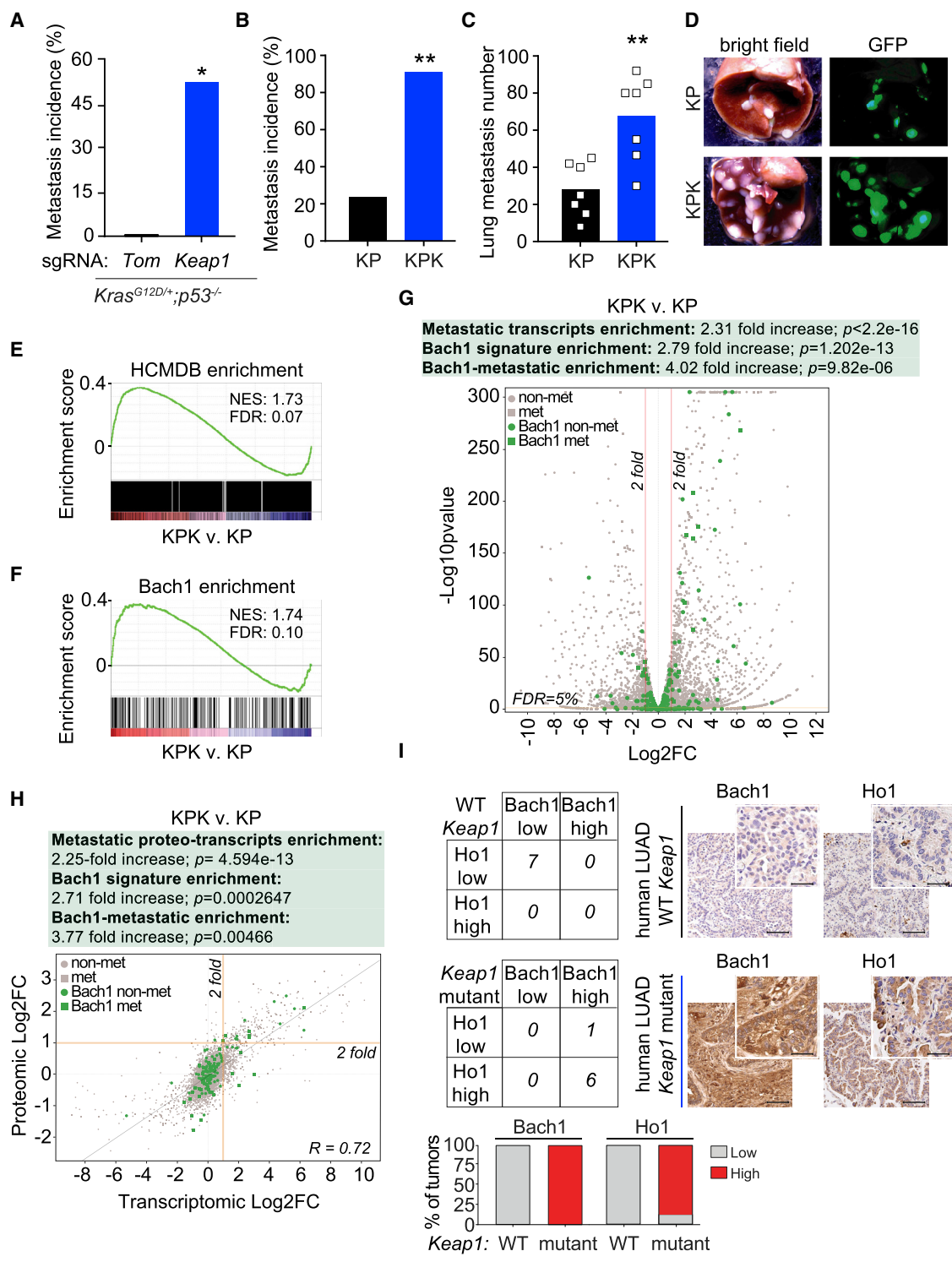


Figure 1. *Keap1* Loss Promotes Cell Migration, Metastasis, and Activation of the Bach1 Transcriptional Program

(A) Metastasis incidence (thoracic and lymph nodes) in sg*Tom* and sg*Keap1* KP mice ($n = 9$ and 8 , respectively) at 21 weeks after intratracheal infection with pSECC lentiviruses.

(B) Metastasis incidence (thoracic and lymph nodes) upon intratracheal implantation of KPK or KP cells ($n = 9$ in each group) at moribund or 100 days after implantation.

(C) Quantification of lung metastasis at 4 weeks after subcutaneous (SQ) implantation of KPK or KP cells expressing GFP reporter ($n = 7$ in each group). Data are presented as means, and squares represent individual data points.

(legend continued on next page)

We studied the molecular mechanisms by which accumulation of Nrf2 promotes metastasis in LUAD. The results of these studies are presented herein.

RESULTS

Keap1 Loss Promotes Cell Migration, Metastasis, and Activation of the Bach1 Transcriptional Program

To study the role of *Keap1* mutations in metastasis, we utilized the KP (*Kras*^{LSL-G12D/+}; *p53*^{flox/flox}) GEMM in combination with a CRISPR/Cas9-based loss-of-function system (Romero et al., 2017; Sánchez-Rivera et al., 2014). KP mice that were intratracheally infected with pSECC lentiviral vectors expressing a single guide RNA (sgRNA) targeting *Keap1* had significantly increased incidence of metastasis as compared to *Keap1* wild type (WT) control animals infected with a control sgRNA (sgTom, targeting tdTomato) (Figure 1A). To determine if the pro-metastatic effect of *Keap1* loss was cell autonomous, we performed *in vitro* assays to measure cell migration properties of KP cells, which were generated from KP-derived lung tumor cells and isogenic *Keap1* knockout (KPK) cells (Romero et al., 2017). In both a Transwell and a scratch assay, KPK cells displayed markedly higher cell migration ability compared to KP cells (Figures S1A and S1B). We next transplanted KP and KPK cells orthotopically into the lungs of syngeneic C57B6/J mice and assessed metastasis formation. KPK cells were more metastatic compared to KP controls without having a significant impact on survival at the time when the mice were sacrificed (Figures 1B, S1C, and S1D). We also subcutaneously transplanted KP and KPK cells in nude mice. Mice implanted with KPK cells displayed significantly higher number of lung metastases compared to mice implanted with KP cells without affecting primary tumor mass (Figures 1C, 1D, and S1E).

To investigate the cellular pathways promoting metastasis in *Keap1* mutant cells, we performed RNA sequencing based transcriptional profiling of KP and KPK cells followed by Gene Set Enrichment Analysis (GSEA). To identify metastatic genes, we took advantage of the Human Cancer Metastasis Database (HCMDb) (Zheng et al., 2018). Our analysis showed a significant enrichment of metastatic genes in KPK compared to KP cells (Figure 1E; Table S1). We also investigated the transcriptional

drivers that could induce the enrichment of metastatic genes. In line with previous observations (Malhotra et al., 2010), the Nrf2 signature was highly enriched in KPK compared to KP cells (Figure S1F; Table S2). However, the Bach1 signature had the highest enrichment score in KPK compared to KP cells (Figure 1F; Table S2), suggesting that the pro-metastatic transcription factor Bach1 could be a driver of the metastatic phenotype of *Keap1* mutant cells.

Next, we analyzed both transcriptomic and proteomic differential expression profiles in KP and KPK cells. In all differential expression analyses, whether transcriptomic or proteomic, we applied a 5% FDR (false discovery rate) cutoff as well as a 2-fold change threshold. We detected a 2.31-, a 2.79-, and a 4.02-fold increase in metastatic transcripts, Bach1 transcriptional targets, and Bach1 targets that are implicated in metastasis, respectively (Figure 1G; Table S3). In parallel, we performed tandem mass tags-based proteomic analysis in KPK compared to KP cells (Figures S1G and S1H). We detected a 2.13-, 2.81-, and a 4.5-fold increase in metastatic proteins, proteins encoded by Bach1 target genes, and metastatic proteins encoded by Bach1 target genes, respectively. Finally, we performed an integrative multi-omics analysis of the transcriptome and proteome of KP and KPK cells to obtain a high confidence set of pro-metastatic transcripts and proteins that are regulated by Bach1. We analyzed the differentially expressed proteo-transcripts in KPK compared to KP cells and detected a 2.25-, a 2.71-, and a 3.77-fold increase in metastatic proteo-transcripts, Bach1-regulated proteo-transcripts, and Bach1-regulated metastatic proteo-transcripts, respectively (Figure 1H). In the latter two cases, the enrichment was much more pronounced in the upregulated proteo-transcripts (3.47- and 4.6-fold increase) than in the downregulated ones (1.07- and 1.98-fold increase).

Next, we assessed whether the activation of the Bach1 signature corresponded to high levels of Bach1 protein in *Keap1* mutant tumors. To this end, we stained (1) GEMM-derived KP and KPK tumors (from Figure 1A), (2) LUAD patient-derived xenograft (PDX) tumors that were *Keap1* WT or *Keap1* mutant, and (3) primary human LUAD tumors with WT or mutant *Keap1* (Romero et al., 2017). In line with transcriptional and proteomic analysis of KP and KPK cells, we found that all tumors with

(D) Representative bright-field and GFP fluorescent images of lung metastasis from (C).

(E) Upregulation of HCMDb genes in KPK versus KP cells.

(F) Upregulation of Bach1 transcriptional signature in KPK versus KP cells.

(G) A volcano plot comparing the expression of HCMDb genes and Bach1 targets genes between KPK and KP cells. Plotted for each transcript are the negative log₁₀ of the p value and the log₂ of the fold change of gene expression of KPK versus KP cells. The red bars represent fold change values of ±2 and the yellow bar represents an FDR threshold of 5%. Circle data points represent non-metastatic transcripts (non-met); square data points represent metastatic transcripts (met); gray data points represent non-Bach1 target transcripts; green data points represent Bach1 target transcripts. FC, fold change.

(H) Correlation plot between protein and mRNA level changes in KPK versus KP cells. For each of 8,586 mRNA fold changes in KPK versus KP cells (x axis, log₂ scale) the associated protein fold change in KPK versus KP cells is plotted (y axis, log₂ scale). The Pearson correlation coefficient (R square) was 0.72. The yellow bars represent a fold change value of +2 for both mRNA and protein levels. Circle data points represent non-metastatic proteo-transcripts; square data points represent metastatic proteo-transcripts; gray data points represent non-Bach1 target proteo-transcripts; green data points represent Bach1 target proteo-transcripts. FC, fold change.

(I) Contingency tables demonstrating the correlation between Bach1 and Ho1 protein expression in IHC analyses of mutant-*Keap1* versus WT *Keap1* biopsies of human LUAD. *Keap1* status was confirmed in all tumor samples by targeted exome sequencing. The graph shows the percentage of LUAD biopsies with low or high levels of Bach1 and Ho1. Bach1 and Ho1 levels increase in mutant-*Keap1* versus WT *Keap1* biopsies: p = 0.0006 and p = 0.0047 respectively. Right, representative IHC stainings. Scale bars, 100 μM for low magnification (10×) and 25 μM for high magnification (40×).

See also Figure S1 and Tables S1, S2, and S3.

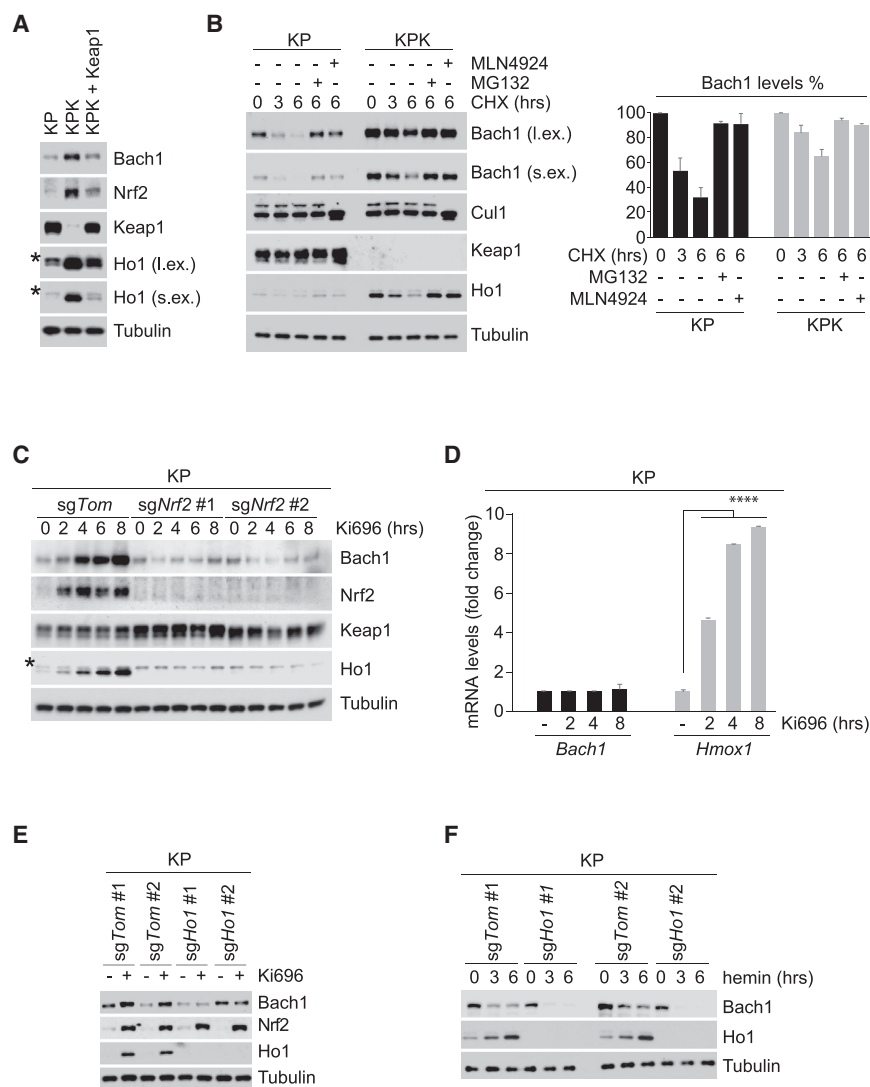


Figure 2. Keap1 Loss Promotes Bach1 Accumulation through Nrf2-Dependent Induction of Ho1

(A) KP, KPK, and Keap1-reconstituted KPK cells were lysed and immunoblotted as indicated. *Denotes a nonspecific band. l.ex., long exposure; s.ex., short exposure.

(B) KP and KPK cells were treated with CHX, collected at the indicated times, lysed, and immunoblotted. Where indicated, KP and KPK cells were pre-treated with either MG132 or MLN4924 30 min before CHX treatment. The graph shows the quantification of Bach1 protein levels. Values are presented as means \pm SEM. l.ex., long exposure; s.ex., short exposure.

(C) KP-sgTom or 2 different KP-sgNrf2 clones were treated with Ki696, collected at the indicated times, lysed, and immunoblotted as indicated. *Denotes a nonspecific band.

(D) KP cells were treated with Ki696 for the indicated times. Relative expression levels of *Bach1* and *Hmx1* genes were determined by qRT-PCR. Values are presented as means \pm SD.

(E) Two different KP-sgTom and KP-sgHo1 clones were treated with Ki696 for 3 h, collected, lysed, and immunoblotted as indicated.

(F) The experiment was performed as in (E), except that cells were treated with hemin for the indicated times.

See also Figure S2.

mutations in *Keap1* displayed higher levels of Bach1 compared to WT controls (Figures 1I, S1I, and S1J).

Keap1 Loss Promotes Bach1 Accumulation through the Nrf2-Dependent Induction of Ho1

The above data suggest that in *Keap1* mutant cells Bach1 protein levels and transcriptional activity are increased. We investigated the molecular mechanisms behind the induction of Bach1 protein levels. First, we analyzed the protein levels of Bach1 in KP and KPK cells and found higher levels of Bach1 in KPK compared to KP cells (Figure 2A), in line with increased Bach1 levels in *Keap1* mutant tumors (Figures 1I, S1I, and S1J). Importantly, reconstitution of Keap1 expression in KPK cells reduced Bach1 expression to the same levels present in KP cells (Figure 2A). Moreover, Bach1 half-life was much longer in KPK than KP cells (Figure 2B), demonstrating that Keap1 loss results in the stabilization of Bach1. Treatment with either MG132 (a proteasome inhibitor) or MLN4924 (a CRL inhibitor) completely blocked Bach1's decay, indicating that Bach1 degradation is

regulated by the proteasome and one or more CRL complexes (Figure 2B). As Keap1 is a substrate receptor of a CRL3 complex, we assessed the possibility that Bach1 could be a novel substrate of CRL3^{Keap1}. Co-immunoprecipitation experiments showed that Keap1 co-immunoprecipitated with Nrf2 and Palb2 (Orthwein et al., 2015), two established substrates of CRL3^{Keap1}, but not with Bach1 (Figure S2A). Similarly, Nrf2 could co-immunoprecipitate Keap1, but not Bach1 (Figure S2B). These results suggest that the augmented levels and stabilization of Bach1 in *Keap1* mutant cells and tumors are not due to Bach1 being a substrate of CRL3^{Keap1}.

Next, we asked if Bach1 accumulation could be driven by Nrf2 accumulation in response to *Keap1* inactivation. To this end, we treated KP cells with Ki696, a small molecule inhibitor of the Keap1-Nrf2 interaction (Davies et al., 2016). As expected, Ki696 treatment led to Nrf2 accumulation as well as a rapid and robust accumulation of Bach1 protein levels with no change in mRNA levels (Figures 2C and 2D). These results combined with a prolonged half-life of Bach1 in KPK cells, indicate that Nrf2 accumulation leads to stabilization of Bach1 through a post-translational mechanism. Notably, in two independent clones of KP cells in which Nrf2 was deleted by CRISPR/Cas9 (Romero et al., 2017), Bach1 did not accumulate upon Ki696 treatment (Figure 2C), indicating that Bach1 stabilization is secondary to Nrf2 activation.

Free heme is a potent oxidative agent that directly binds Bach1 and promotes its proteasomal degradation (Zenke-Kawasaki et al., 2007). In response to stress, Nrf2 accumulates and activates the transcription of genes involved in heme catabolism, including Ho1, the enzyme that catalyzes the first and rate-limiting step in heme degradation (Sun et al., 2004). Thus, we investigated whether Nrf2 accumulation stabilizes Bach1 by inducing Ho1 transcription. As expected, Nrf2 activation by either loss of *Keap1* or Ki696 treatment led to a robust increase of Ho1 both at the mRNA and protein levels (Figures 2A–2D). Using two independent *Ho1* knockout KP clones (Figure S2C), we observed that Ki696-mediated Nrf2 stabilization did not result in an increase of Bach1 (Figure 2E), indicating that the stabilization of Bach1 triggered by Nrf2 accumulation is likely due to enhanced Ho1-dependent degradation of heme. Moreover, the degradation of Bach1 induced by treatment with hemin (Fe³⁺ heme) was dramatically increased in *Ho1* null cells compared to *Ho1* WT cells (Figure 2F), likely because of the lack of Ho1-mediated degradation of hemin in *Ho1* null cells. To further confirm these results, we treated KP and KPK cells with hemin in the presence or absence of TinPPIX (Tin Protoporphyrin IX), a selective inhibitor of Ho1 enzymatic activity (Morita et al., 1995). Similar to what we observed in *Ho1* null cells, pharmacological inhibition of Ho1 led to accelerated Bach1 degradation (Figures S2D and S2E).

Next, we assessed Ho1 protein levels in primary human LUADs with WT or mutant *Keap1*. Human tumors with *Keap1* mutations had both high levels of Bach1 and Ho1 as compared to *Keap1* WT tumors (Figure 1I), demonstrating a positive correlation between levels of Ho1 and Bach1 in human LUAD, in agreement with our biochemical studies.

Together, these results strongly indicate that cancer cells with genetic or pharmacological activation of Nrf2 have increased Bach1 levels through an Ho1-dependent mechanism.

Fbxo22 Mediates the Heme-Induced Degradation of Bach1

To identify the ubiquitin ligase that mediates the heme-induced degradation of Bach1, we performed immunopurifications of Bach1 expressed in human HEK293T cells in the presence or absence of hemin, followed by mass spectrometry analysis. The Bach1 interactome showed nine substrate receptors of CRL complexes, as well as Skp1, an assembly factor of the CRL1 complex (Figure S3A). We ectopically expressed in HEK293T cells seven FLAG-tagged CRL substrate receptors, as well as FLAG-tagged Hoi1, a ubiquitin ligase previously reported to target Bach1 for degradation (Zenke-Kawasaki et al., 2007). Immunoprecipitation of these proteins showed Fbxo22, a CRL1 substrate receptor, as the most efficient and selective interactor of endogenous Bach1 (Figure 3A), in agreement with the highest number of Fbxo22-corresponding peptides in the mass spectrometry analysis (Figure S3A). The interaction between Bach1 and Fbxo22 was also confirmed at the endogenous levels (Figure 3B). Interestingly, Bach1 interacted more robustly with Fbxo22 in KP cells than in KPK cells, the latter having presumably less intracellular heme, due to the increased expression of Ho1. Accordingly, addition of hemin increased the binding between Bach1 and Fbxo22 (Figures 3B, S3A, and S3B). These re-

sults suggest that heme induces the degradation of Bach1 by increasing its interaction with Fbxo22.

Next, we assessed if Fbxo22 manipulation affected Bach1 stability. Doxycycline (dox)-inducible knock down of *Fbxo22* led to stabilization of Bach1 both in human and mouse LUAD cell lines in the presence of either hemin, cycloheximide (CHX) or TinPPIX (Figures 3C and S3C–S3F). Additionally, we observed complete stabilization of Bach1 in *Fbxo22* knockout cells treated with either hemin or CHX (Figures 3D and S3G–S3I).

We then mapped the Fbxo22 binding motif in Bach1 (i.e., the Bach1 degradation motif or degron). After examining multiple Bach1 deletion mutants for their abilities to bind Fbxo22, we narrowed down the degron to a region between amino acids 6–20, a region highly conserved in Bach1 orthologs (Figures S4A–S4D). Alanine scanning mutagenesis of amino acids 6–20 showed that Bach1(F9A), Bach1(Y11A), Bach1(S13A), as well as Bach1(Y11F), Bach1(S13D), and Bach1(S13E), but no other single amino acid substitution mutants, failed to co-immunoprecipitate with endogenous Fbxo22 (Figures 3E and S4E–S4G), indicating that residues 9, 11, and 13 of Bach1 are necessary for its binding to Fbxo22. Interestingly, Bach1(Y11H), a mutant mimicking a cancer-related mutation (TCGA: TCGA-LN-A7HY-01), was also unable to bind Fbxo22 (Figure 3E).

Next, we generated human LUAD cell lines stably expressing a dox-inducible construct for WT Bach1 or Bach1(Y11F). In agreement with its inability to bind Fbxo22, Bach1(Y11F) exhibited a half-life longer than WT Bach1 both in untreated and hemin-treated cells (Figures S5A–S5D). Moreover, Fbxo22 overexpression drastically decreased the half-life of WT Bach1, but not of Bach1(Y11F) (Figures 3F and S5E). Virtually identical results were obtained in mouse *Bach1* null KP cells stably expressing both exogenous Fbxo22 and a dox-inducible construct for either WT Bach1 or Bach1(Y11F) (Figures S5F–S5I).

Overall, these results demonstrate that Fbxo22 mediates the heme-dependent degradation of Bach1.

Fbxo22 Depletion Activates Bach1 Transcriptional Program and Promotes Cell Migration

Given the role of Bach1 in promoting metastasis, we examined whether Bach1 accumulation in response to *Fbxo22* knock down activates the Bach1-prometastatic transcriptional program, which we observed in KPK cells (Figure 1). To this end, we depleted Fbxo22 in both KP and KPK cells and then performed transcriptional profiling by RNA sequencing. In line with the increased levels of Bach1 in *Fbxo22* knockdown KP cells (Figure S3E), we found the Bach1 transcriptional signature was highly enriched in Fbxo22-depleted KP cells compared to control KP cells (Figure S6A; Table S4). Bach1 targets were differentially expressed in Fbxo22-depleted KP cells compared to control KP cells at 5% FDR (Figure 4A; Table S5). A total of 29 Bach1 targets were significantly upregulated by at least 2-fold, while 7 were significantly downregulated by at least 2-fold. Fourteen of the 29 upregulated genes and only 1 out of the 7 downregulated genes are known to be associated with metastasis. In contrast to KP cells, we did not observe a significant enrichment of the Bach1 signature when *Fbxo22* was silenced in KPK cells (Figure 4B; Table S5), which is consistent with the already high levels of Bach1 in KPK cells (Figure 2).

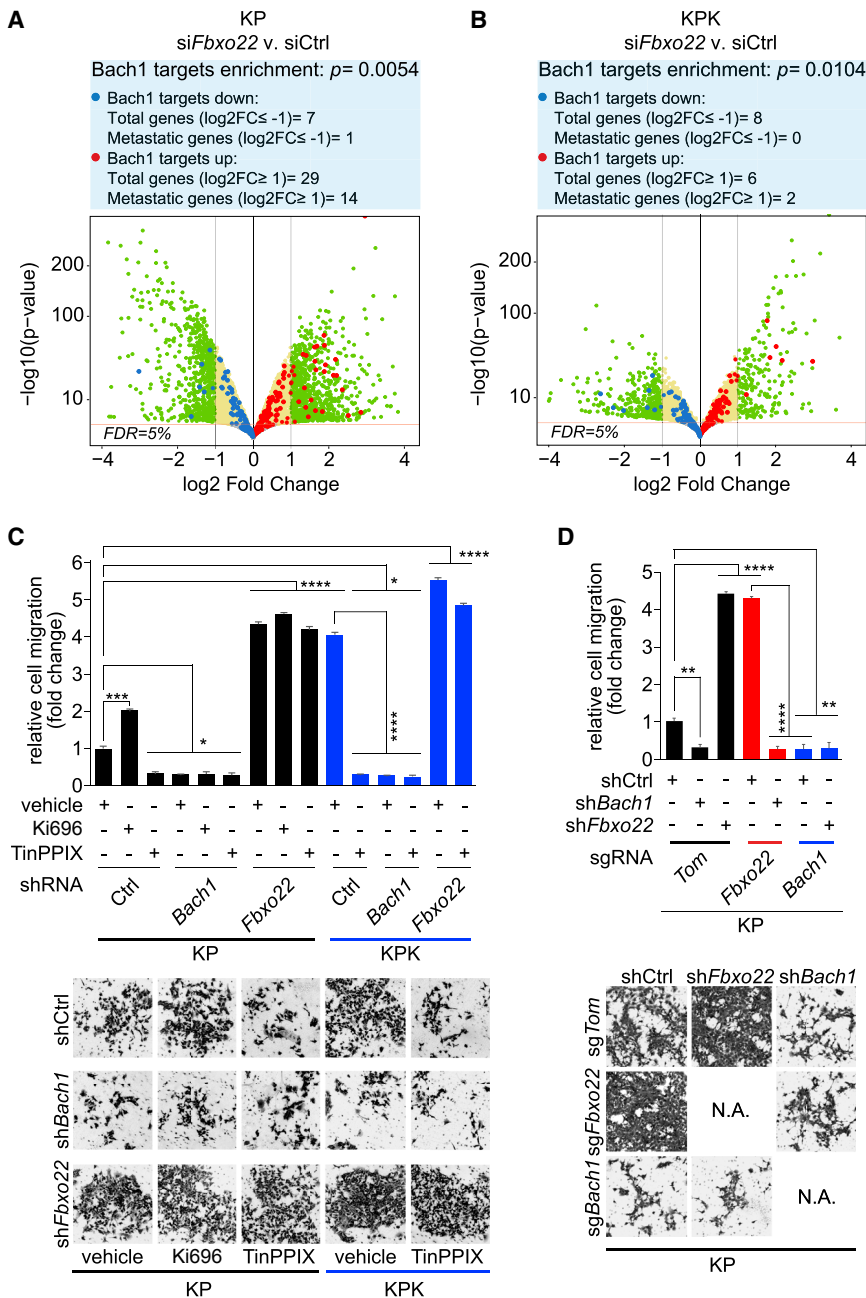


Figure 4. Fbxo22 Depletion Activates Bach1 Transcriptional Program and Promotes Cell Migration

(A) Volcano plot comparing the expression of Bach1 signature genes in KP cells transfected with either a non-targeting small interfering RNA (siRNA) (siCtrl) or siFbxo22. Plotted for each gene are the negative log10 of the p value and the log2 of the fold change of gene expression of KP-siFbxo22 cells relative to KP-siCtrl cells. The green dots represent genes with fold change values of ± 2 , and the red bar represents a FDR threshold of 5%. The blue dots represent downregulated Bach1 target genes, while the red dots represent upregulated Bach1 target genes. The enrichment of transcripts was calculated considering the transcripts with at least 2-fold change at 5% FDR. (B) The experiment was performed as in (A), except that the volcano plot compares the expression of Bach1 signature genes in KPK-siFbxo22 cells versus KPK-siCtrl cells.

(C) KP and KPK cells infected with lentiviruses expressing either a dox-inducible, non-targeting shRNA (shCtrl) or dox-inducible shRNAs targeting either *Bach1* (sh*Bach1*) or *Fbxo22* (sh*Fbxo22*). Forty-eight hours after dox induction, cells were treated with either Ki696 or TinPPIX for 24 h. Cells were then tested for migration in a Boyden chamber assay over a 12-h period. Next, cells migrated on the bottom of the Transwells were fixed, stained, and counted in 5 different fields per well. The graph shows quantification from 3 technical replicates of a representative experiment. Bottom: representative images of migrated cells. Values are presented as means \pm SEM.

(D) KP-sg*Tom*, KP-sg*Fbxo22*, and KP-sg*Bach1* cells transduced with lentiviruses expressing a dox-inducible shCtrl, sh*Bach1*, or sh*Fbxo22* were treated with dox for 72 h and tested for migration as in (C). Values are presented as means \pm SEM.

See also Figure S6 and Tables S4 and S5.

and pharmacologically that Keap1 and Fbxo22 inhibit a Bach1-dependent cell migratory phenotype, whereas Nrf2 and Ho1 promote it.

Bach1 Promotes Whereas Ho1 Inhibition Decreases Metastasis Formation

Next, we investigated the impact of the Fbxo22-Bach1 axis *in vivo*. To this end, we assessed metastasis formation in nude mice subcutaneously transplanted with KP or KPK cells expressing inducible sh*Bach1*, sh*Fbxo22*, or shCtrl. In line with our previous results (Figure 1C), mice implanted with KPK-shCtrl cells had

increased metastases compared to mice implanted with KP-shCtrl cells (Figure 5A). Importantly, depletion of Bach1 reduced metastases of both KP and KPK tumors and, conversely, depletion of Fbxo22 increased metastases in mice with KP tumors to the same extent as observed in

mice with KPK tumors (Figure 5A). The differences in metastatic potential were not due to increased tumor growth (Figure S7A). To assess the effects of Fbxo22 loss in an autochthonous lung tumorigenesis setting, we used the KP GEMM. Specifically, we generated bi-functional uSEC (U6::sgRNA-EFS::Cre) lentiviruses expressing Cre recombinase and sgRNAs against *Fbxo22*, *Keap1*, or *tdTomato*, which were delivered intratracheally in the lungs of KP;*Rosa26*^{LSL-Cas9-2a-GFP} mice (Figure 5B). We observed a significant increase in the incidence of metastasis in both sg*Fbxo22* and sg*Keap1* animals as compared to sg*Tom* control mice (Figure 5C). Furthermore, tumor burden in

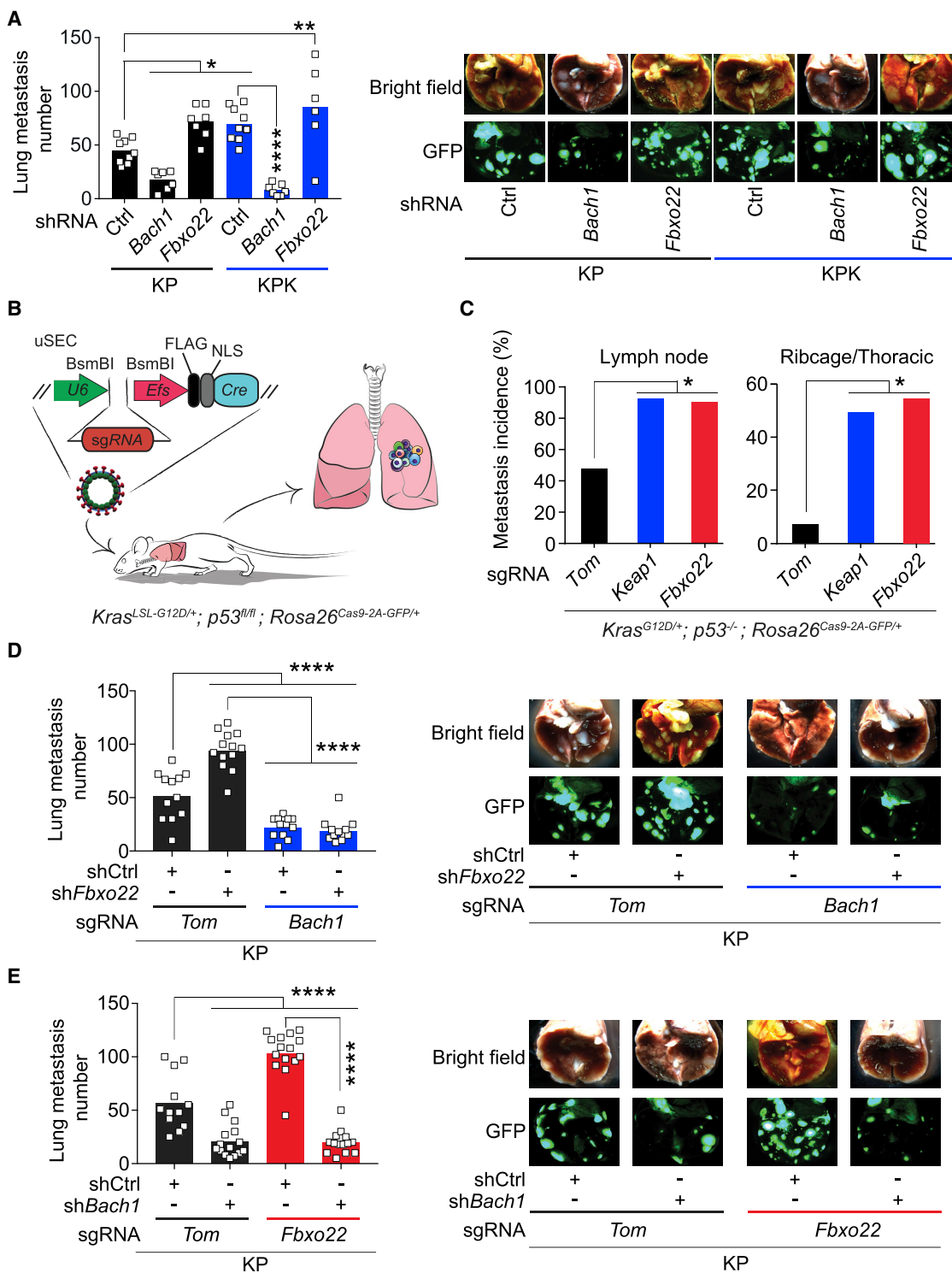


Figure 5. Bach1 Promotes Metastasis

(A) Quantification of lung metastases at 4 weeks after SQ implantation of KP and KPK cells expressing a GFP-luciferase reporter and transduced with lentiviruses expressing a dox-inducible shCtrl, shBach1, or shFbxo22 (from left to right, n = 9, 7, 7, 9, 7, and 6). Mice were put on a dox diet 10 days after implantation. Data are presented as means, and squares represent individual data points. Right, representative brightfield and GFP fluorescent images of lung metastasis.

(B) Schematic representation of *Kras^{LSL-G12D/+}; p53^{fl/fl}* (KP) mice intratracheally infected with uSEC lentiviruses containing sgTom, sgKeap1, or sgFbxo22.

(C) Metastasis incidence in sgTom, sgKeap1, or sgFbxo22 mice (n = 12, 10, and 9 respectively) at 21 weeks after intratracheal infection with uSEC lentiviruses.

(legend continued on next page)

sg*Fbxo22* and sg*Keap1* mice were significantly higher than sg*Tom* mice (Figure S7B). Using immunohistochemistry (IHC), we confirmed that tumors of sg*Fbxo22* mice stained negative for Fbxo22 and expressed high Bach1 levels, while tumors from sg*Tom* mice stained positive for Fbxo22 and displayed low Bach1 levels (Figure S7C).

Next, we assessed metastasis formation in nude mice subcutaneously transplanted with either control (sg*Tom*), *Fbxo22* null, or *Bach1* null KP cells expressing inducible sh*Bach1*, sh*Fbxo22*, or shCtrl. In line with our previous results, implantation of Bach1-deficient cells decreased metastasis compared to mice implanted with control cells, while *Fbxo22*-deficient cells increased it (Figures 5D and 5E). Importantly, concomitant depletion of Bach1 drastically reduced the formation of metastases induced by *Fbxo22* loss (Figures 5D and 5E), suggesting that the increased metastatic rate induced by *Fbxo22* depletion is mediated by Bach1. No significant impact on primary tumor growth was observed (Figures S7D and S7E).

Finally, we analyzed metastasis formation in nude mice subcutaneously implanted with *Bach1* knockout KP cells stably overexpressing both Fbxo22 and an inducible construct for either WT Bach1 or Bach1(Y11F). Bach1 overexpression (either WT or the Y11F mutant) induced a dramatic increase in the number of metastases compared to *Bach1* null cells (Figure 6A). Concomitant overexpression of Fbxo22 significantly decreased metastases induced by WT Bach1 (Figure 6A). Conversely, Fbxo22 failed to reduce metastasis formation in Bach1(Y11F)-expressing cells (Figure 6A), likely due to Fbxo22's inability to bind and degrade this mutant (Figure S5I). No significant impact on primary tumor growth was observed (Figure S7F).

In vitro, TinPPIX treatment triggers Bach1 destabilization and decreases cell migration both in KP and KPK cells. These results prompted us to explore whether inhibition of Ho1 would suppress metastasis formation. To this end, we assessed metastasis formation in nude mice subcutaneously transplanted with KP or KPK cells expressing inducible sh*Fbxo22* or shCtrl. Once primary tumors were established, we treated animals for 14 days with either vehicle or ZnPPIX, an Ho1 inhibitor (Doi et al., 1999; Fang et al., 2003). In line with our previous results, KPK-shCtrl and KP-sh*Fbxo22* cells metastasized more than KP-shCtrl cells (Figure 6B). Ho1 inhibition by ZnPPIX treatment significantly reduced metastasis in both KP and KPK models (Figure 6B) without having any significant impact on primary tumor weight (Figure S7G). Strikingly, the Ho1 inhibitor had no effect on the metastatic potential of KP-sh*Fbxo22* and KPK-sh*Fbxo22* cells (Figure 6B), suggesting that Ho1 inhibition reduced metastasis formation through the promotion of the Fbxo22-mediated degradation of Bach1.

Altogether, these results indicate that Bach1 accumulation by either *Keap1* or *Fbxo22* loss induces metastasis formation. In addition, pharmacological inhibition of Ho1 decreases metastasis formation by promoting the Fbxo22-mediated degradation of Bach1.

Bach1 Levels and Its Transcriptional Signature Is Associated with Poor Survival, Advanced Clinical Stage and Grade, and Presence of Metastases in Human LUAD

Next, we assessed the levels of Bach1 and Ho1 in tissue microarrays generated from human LUAD primary tumor samples with matching metastasis. We found that both Bach1 and Ho1 levels were significantly increased in LUAD metastases compared to matched primary tumors ($p = 0.0048$ and $p = 0.0154$, respectively) (Figure 7A). Moreover, there was a significant correlation between high Ho1 and high Bach1 levels in metastases ($p = 0.0004$) (Figure 7A). An analysis of the Bach1 signature (Bach1 MutSig) in a dataset of human LUAD patient samples ($n = 548$) (Cancer Genome Atlas Research Network, 2014) showed a significant enrichment of the Bach1 signature in high-grade tumors (Figure 7B) and late-stage disease (Figure 7C). Furthermore, the Bach1 signature was significantly enriched in primary tumors from LUAD patients with lymph node metastasis as compared to patients with no metastasis (Figure 7D). Ranking tumors by the strength of their correlation with the Bach1 signature allowed for stratification of all TCGA subjects with LUAD into two subpopulations. The subpopulation with the highest Bach1 correlation displayed significantly shorter survival compared to the rest of the cohort (Figure 7E). Notably, this Bach1 signature was found to be independently prognostic in the TCGA LUAD cohort while controlling for other clinical covariates in a Cox proportional-hazards model (Table S6), in which higher enrichment for the signature was associated with significantly worse survival. Finally, in agreement with the enrichment of the Bach1 signature with aggressive disease (stage, grade and metastasis), the Bach1 signature was prognostic for stage (III/IV versus I/II), grade (T3/T4 versus T1/2), and lymph node metastasis (N1/N2 versus N0) (Table S6).

Taken together, these data suggest that high Bach1 levels in LUAD are associated with increased metastasis and poor survival.

DISCUSSION

Metastasis is the primary cause of death in cancer patients. Approximately 30% of NSCLC patients harbor either inactivating somatic mutations in *Keap1* or mutations in *Nfe2l2*, respectively, leading to stabilization of Nrf2. The impact of these mutations on

(D) Quantification of lung metastases at 4 weeks after SQ implantation of KP-sg*Tom* and KP-sg*Bach1* cells expressing a GFP-luciferase reporter and transduced with lentiviruses expressing either a dox-inducible shCtrl or sh*Fbxo22* (from left to right, $n = 12, 13, 13,$ and 12). Mice were put on a dox diet 10 days after implantation. Data are presented as means, and squares represent individual data points. Right: representative bright-field and GFP fluorescent images of lung metastasis.

(E) Quantification of lung metastases at 4 weeks after SQ implantation of KP-sg*Tom* and KP-sg*Fbxo22* cells expressing a GFP-luciferase reporter and transduced with lentiviruses expressing either a dox-inducible shCtrl or sh*Bach1* (from left to right, $n = 12, 15, 15,$ and 14). Mice were put on a dox diet 10 days after implantation. Data are presented as means, and squares represent individual data points. Right: representative bright-field and GFP fluorescent images of lung metastasis.

See also Figure S7.

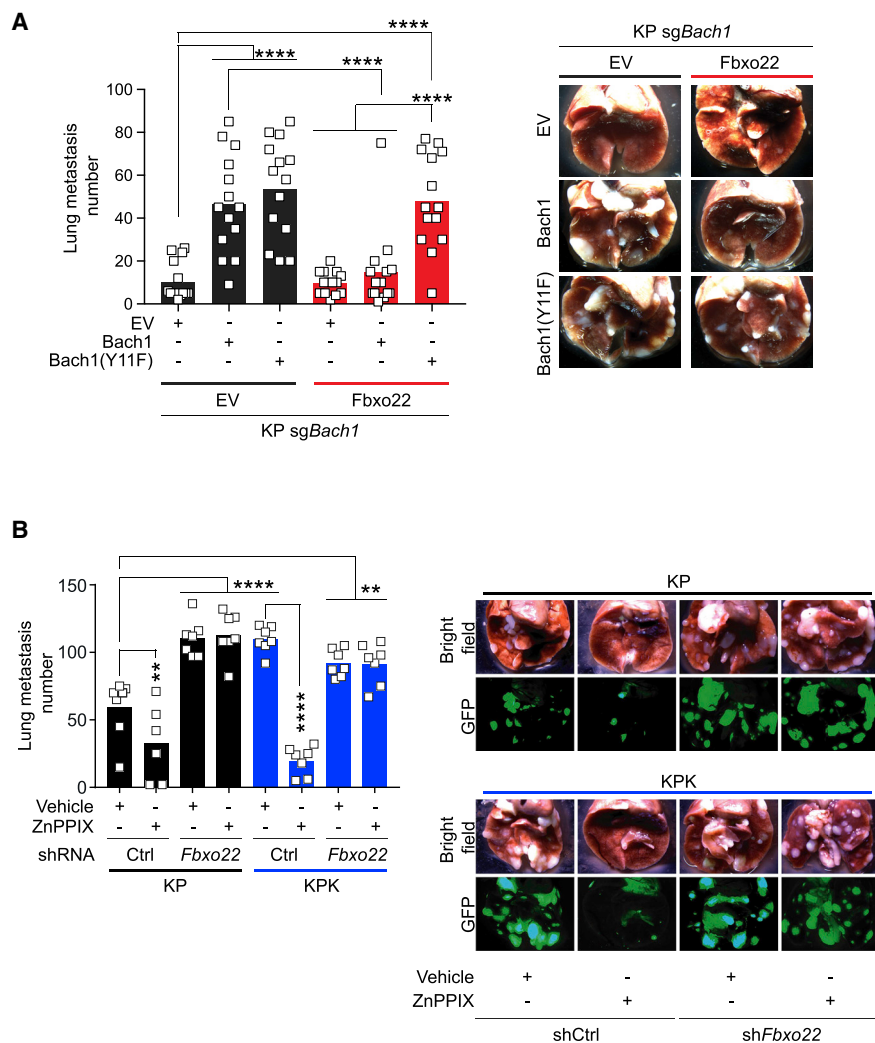


Figure 6. Fbxo22 Overexpression or Ho1 Inhibition Blocks Bach1-Driven Metastasis

(A) Quantification of lung metastases at 4 weeks after SQ implantation of KP-*sgBach1* cells infected with lentiviruses expressing either EV or Fbxo22 in combination with lentiviruses expressing a dox-inducible EV, WT Bach1, or Bach1(Y11F) ($n = 14$ in each group). Mice were put on a dox diet 10 days after implantation. Data are presented as means, and squares represent individual data points. Right: representative bright-field images of lung metastases.

(B) Quantification of lung metastases at 4 weeks after SQ implantation of KP and KPK cells expressing a GFP-luciferase reporter and infected with lentiviruses expressing either a dox-inducible shCtrl or a dox-inducible shFbxo22. Mice were put on a dox diet 10 days after implantation. Two weeks after implantation, mice were randomized and daily injected for 14 days with either vehicle or ZnPPiX 40 mg/kg (from left to right, $n = 7, 6, 7, 7, 7, 7, 7, 7$). Data are presented as means, and squares represent individual data points. Right: representative bright-field and GFP fluorescent images of lung metastases. See also Figure S7.

metastatic genes, such as CXCR4 and MMPs (Lee et al., 2013; Liang et al., 2012; Yun et al., 2011). Notably, we found that in LUAD patients, the expression of Bach1 target genes is associated with high-grade, advanced-stage, and highly metastatic disease, as well as shortened survival.

Mechanistically, we dissected the molecular events regulating Bach1 stability. It has been shown that Bach1 degradation is promoted by free heme

(Zenke-Kawasaki et al., 2007). We found that the heme-induced degradation of Bach1 is mediated by Fbxo22, a substrate receptor of a CRL1 complex. We showed that heme promotes the physical interaction between Bach1 and Fbxo22, which represents the long-sought molecular mechanism by which heme triggers the elimination of Bach1. Two other ubiquitin ligases (Hoil1 and Fbxl17) have been proposed to target Bach1 for degradation in a heme-dependent manner (Tan et al., 2013; Zenke-Kawasaki et al., 2007). We did not detect any interaction between Bach1 and Hoil1, but, in agreement with a large proteomic study by (Huttlin et al., 2017), we observed that Bach1 binds to Fbxl17, although not as stably as to Fbxo22. Moreover, in contrast to the binding to Fbxo22, the interaction with Fbxl17 decreased upon hemin treatment. Fbxl17 has recently been shown to selectively ubiquitylates BTB dimers of aberrant composition (Mena et al., 2018), suggesting that Fbxl17 targets Bach1 only when it is in complex with the wrong BTB protein.

It is generally believed that the Bach1-mediated repression of Maf-regulated genes is dominant over the Nrf2-mediated activation of these genes (Reichard et al., 2007). Our data suggest that

the formation of metastasis in lung cancer patients has remained unclear. Nrf2 activation has been shown to promote cell migration *in vitro* (Wang et al., 2016; Zhang et al., 2012) and metastasis in a hepatocellular carcinoma mouse model (Zhang et al., 2015). Moreover, in a Kras-driven LUAD GEMM, *Keap1* loss leads to the appearance of high-grade invasive adenocarcinomas that are typically associated with increased metastases (Winslow et al., 2011). Similarly, loss of *Keap1* in LUAD patients is associated with high-grade and late-stage disease and shortened survival (Romero et al., 2017), which might be caused by an increased rate of metastasis in these patients. Conversely, other studies in lung carcinoma mouse models, indicate that NRF2 has anti-metastatic properties (Hiramoto et al., 2014; Suzuki and Yamamoto, 2015). Our results show that *Keap1* loss induces the activation of a pro-metastatic transcriptional program and a dramatic increase of the metastatic phenotype in LUAD mouse models. Activation of the metastatic program induced by *Keap1* loss is driven by the accumulation of Bach1, which has been described, particularly in breast cancer, as a key pro-metastatic transcription factor that promotes the transcription of critical

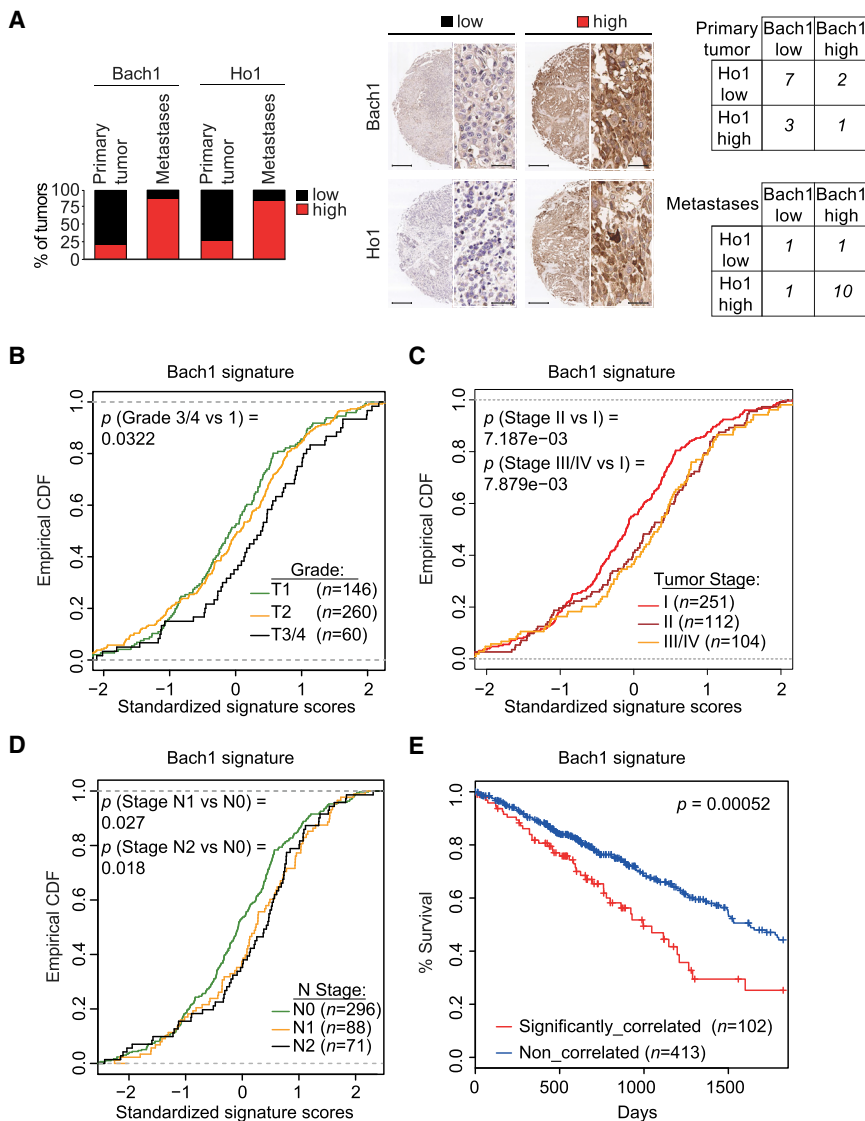


Figure 7. Bach1 Levels and Its Transcriptional Signature Are Associated with Poor Survival, Advanced Clinical Stage and Grade, and Presence of Metastases in Human LUAD

(A) The graph shows the percentage of primary human LUAD samples with matching metastasis (n = 13) displaying low or high levels of Bach1 and Ho1. Middle: representative IHCs. Scale bars, 330 μ M for low magnification (3 \times) and 25 μ M for high magnification (40 \times). Right: contingency tables demonstrating the correlation between Ho1 and Bach1 expression in primary tumors (top) and matching metastases (bottom).

(B) Empirical cumulative distribution function (CDF) plots showing correlation of individual tumors with the Bach1 signature across various tumor grades within the TCGA LUAD cohort.

(C) CDF plots showing correlation of individual tumors with the Bach1 signature across various clinical stages within the TCGA LUAD cohort.

(D) CDF plots showing the correlation of individual tumors with Bach1 signature in primary tumors within the TCGA LUAD cohort with lymph node metastasis (N1, N2) as compared to cohort with no metastasis (N0).

(E) Kaplan-Meier survival curves comparing subjects in the TCGA LUAD cohort stratified by correlation with Bach1 signature. Tumor samples were binned according to their gene expression correlation with Bach1 signature. Subjects harboring the top 20% (n = 102) most correlated tumors exhibited significantly decreased survival as compared to the remaining subjects (n = 413) from the TCGA LUAD cohort. See also Table S6.

of gastric cancers, hepatomas, and sarcomas (Doi et al., 1999; Fang et al., 2003; Shang et al., 2015; Tanaka et al., 2003). Overall, our data suggest that drugs targeting the heme pathway might represent a novel therapeutic avenue in LUAD patients with alterations in the

unscheduled Nrf2 activation is able to override Bach1 repression and activate the transcription of antioxidant genes even in the presence of high levels Bach1. At the same time, stabilized Bach1 triggers the activation of other targets, including key pro-metastatic genes.

Notably, we found that, upon *Keap1* loss, Bach1 protein stabilization is induced by the Nrf2-dependent upregulating of Ho1 that, presumably, reduces the levels of free heme. Accordingly, pharmacologic inhibition of Ho1 induces the Fbxo22-dependent degradation of Bach1, resulting in the reduction of cell migration and metastasis. Consistent with our results, Ho1 has been found to be overexpressed in various tumors, to facilitates cancer cell growth and survival, and to promote tumor angiogenesis and metastasis (Dey et al., 2015; Sunamura et al., 2003; Was et al., 2006). Moreover, the efficacy of targeting Ho1 has been proven in animal models. For example, the administration of ZnPPiX significantly suppresses the growth

Keap1-Nrf2 pathway, particularly those in which it is necessary to prevent tumor dissemination. We also speculate that the activation of Bach1 metastatic program is also frequently present in other cancers with genetic, epigenetic, or post-transcriptional alterations in the Keap1-Nrf2 pathway (Cancer Genome Atlas Research Network, 2012; Goldstein et al., 2016; Hanada et al., 2012; Jaramillo and Zhang, 2013; Muscarella et al., 2011). Thus, we hypothesize that the mechanisms we have identified in *Keap1* mutant LUAD tumors may offer new therapeutic opportunities to inhibit metastasis in these cancers as well.

Our findings are complementary and in agreement with the results by Wiel et al. (2019), published in this issue of *Cell*, who found that supplementing the diet of mice harboring lung tumors with either a pharmacological (N-acetylcysteine) or dietary (vitamin E) antioxidant, promotes metastasis by increasing the intracellular levels of Bach1.

In summary, we identified a molecular mechanism by which mutations in the Keap1-Nrf2 axis promotes metastasis. Specifically, activated Nrf2 inhibits the Fbxo22-dependent degradation of Bach1 via induction of Ho1 expression. Notably, we show that lung cancer cells with high levels of Nrf2 display also high levels of Bach1, the latter promoting metastasis through activation of pro-metastatic genes transcription.

STAR★METHODS

Detailed methods are provided in the online version of this paper and include the following:

- [KEY RESOURCES TABLE](#)
- [LEAD CONTACT AND MATERIALS AVAILABILITY](#)
- [EXPERIMENTAL MODEL AND SUBJECT DETAILS](#)
 - Animal experiments
 - Cell Culture Procedures
 - Human lung cancer with matched lymph node metastasis tissue array, human clinical lung cancer samples and Patient derived xenografts (PDXs)
- [METHOD DETAILS](#)
 - CRISPR genome editing
 - Gene Set Enrichment Analysis
 - Gene Silencing by siRNA
 - Human clinical data analyses
 - Immunoprecipitation and immunoblotting
 - Immunohistochemistry and immunofluorescence
 - Lentivirus-Mediated gene transfer
 - Mass Spectrometry
 - Plasmids
 - Proteomics Data Analysis
 - Scratch Assay
 - shRNA cloning and cell line generation
 - Tandem Mass Tag
 - Transcriptomics Data Analysis
 - Transwell Assays
 - Volcano and Scatterplots
- [QUANTIFICATION AND STATISTICAL ANALYSIS](#)
- [DATA AND CODE AVAILABILITY](#)

SUPPLEMENTAL INFORMATION

Supplemental Information can be found online at <https://doi.org/10.1016/j.cell.2019.06.003>.

ACKNOWLEDGMENTS

We thank L. Farina, A. Faustin, H. Shapiro, and Y. Higa (for their help), H. Zhou (for bioinformatic support), W. Harper (for reagents), Craig Thomas (for providing Ki696) the NYU Genome Technology Center, the NYU Center for Biospecimen Research and Development (NCBRD), and the NYU Mass Spectrometric Facility (NMSF) (partially supported by the Cancer Center Support Grant P30CA016087). This work was funded by grants from the NIH (R01CA76584 and R01GM57587 to M.P., T32HL007151 to S.E.L.B., and K22CA201088, R37CA222504, and R01CA227649 to T.P.), NMSF (S10OD010582), and NCBRD (S10OD01058 and S10OD018338), and fellowships from the American Italian Cancer Foundation (AICF) and Associazione Italiana per la Ricerca sul Cancro co-funded by the European Union (AIRC/Marie Curie) to L.L. V.I.S was supported by the Wenner-Gren foundations and the Swedish Society of Medicine. T.P. is supported by an American Can-

cer Society Research Scholar Grant (RSG-17-200-01-TBE). M.P. is grateful to T.M. Thor for continuous support. M.P. is an Investigator with the Howard Hughes Medical Institute.

AUTHOR CONTRIBUTIONS

L.L. conceived and directed the study, designed, and performed most experiments. S.E.L.B., H.H., and T.R.K. helped with some experiments. S.J., M.A., A.J.B., and A.T. performed the bioinformatic analyses. H.I.P. provided human cancer samples. B.U. performed the mass spectrometry analysis. V.I.S. provided conceptual advice and helped with some experiments. T.P. provided conceptual advice and supervised the study. M.P. directed and coordinated the study, designed the research, and oversaw the results. L.L. and M.P. wrote the manuscript with comments from all authors.

DECLARATION OF INTERESTS

M.P. is a member of the advisory boards of Cullgen Inc. and Kymera Therapeutics. He is also a consultant for BeyondSpring Pharmaceuticals.

Received: November 26, 2018

Revised: March 19, 2019

Accepted: June 3, 2019

Published: June 26, 2019

REFERENCES

- Anders, S., Pyl, P.T., and Huber, W. (2015). HTSeq—a Python framework to work with high-throughput sequencing data. *Bioinformatics* *31*, 166–169.
- Bar, J., Herbst, R.S., and Onn, A. (2008). Multitargeted inhibitors in lung cancer: new clinical data. *Clin. Lung Cancer* *9* (Suppl 3), S92–S99.
- Barbie, D.A., Tamayo, P., Boehm, J.S., Kim, S.Y., Moody, S.E., Dunn, I.F., Schinzel, A.C., Sandy, P., Meylan, E., Scholl, C., et al. (2009). Systematic RNA interference reveals that oncogenic KRAS-driven cancers require TBK1. *Nature* *462*, 108–112.
- Benjamini, Y., Drai, D., Elmer, G., Kafkafi, N., and Golani, I. (2001). Controlling the false discovery rate in behavior genetics research. *Behav. Brain Res.* *125*, 279–284.
- Bhardwaj, A., Yang, Y., Ueberheide, B., and Smith, S. (2017). Whole proteome analysis of human tankyrase knockout cells reveals targets of tankyrase-mediated degradation. *Nat. Commun.* *8*, 2214.
- Brady, J.J., Chuang, C.H., Greenside, P.G., Rogers, Z.N., Murray, C.W., Caswell, D.R., Hartmann, U., Connolly, A.J., Sweet-Cordero, E.A., Kundaje, A., and Winslow, M.M. (2016). An Arntl2-Driven Secretome Enables Lung Adenocarcinoma Metastatic Self-Sufficiency. *Cancer Cell* *29*, 697–710.
- Campbell, J.D., Alexandrov, A., Kim, J., Wala, J., Berger, A.H., Pedamallu, C.S., Shukla, S.A., Guo, G., Brooks, A.N., Murray, B.A., et al.; Cancer Genome Atlas Research Network (2016). Distinct patterns of somatic genome alterations in lung adenocarcinomas and squamous cell carcinomas. *Nat. Genet.* *48*, 607–616.
- Cancer Genome Atlas Research Network (2012). Comprehensive genomic characterization of squamous cell lung cancers. *Nature* *489*, 519–525.
- Cancer Genome Atlas Research Network (2014). Comprehensive molecular profiling of lung adenocarcinoma. *Nature* *511*, 543–550.
- Carter, S.L., Cibulskis, K., Helman, E., McKenna, A., Shen, H., Zack, T., Laird, P.W., Onofrio, R.C., Winckler, W., Weir, B.A., et al. (2012). Absolute quantification of somatic DNA alterations in human cancer. *Nat. Biotechnol.* *30*, 413–421.
- Caswell, D.R., Chuang, C.H., Yang, D., Chiou, S.H., Cheemalavagu, S., Kim-Kiselak, C., Connolly, A., and Winslow, M.M. (2014). Obligate progression precedes lung adenocarcinoma dissemination. *Cancer Discov.* *4*, 781–789.
- Chuang, C.H., Greenside, P.G., Rogers, Z.N., Brady, J.J., Yang, D., Ma, R.K., Caswell, D.R., Chiou, S.H., Winters, A.F., Grüner, B.M., et al. (2017). Molecular

- definition of a metastatic lung cancer state reveals a targetable CD109-Janus kinase-Stat axis. *Nat. Med.* **23**, 291–300.
- Cox, J., and Mann, M. (2008). MaxQuant enables high peptide identification rates, individualized p.p.b.-range mass accuracies and proteome-wide protein quantification. *Nat. Biotechnol.* **26**, 1367–1372.
- Cox, J., Neuhauser, N., Michalski, A., Scheltema, R.A., Olsen, J.V., and Mann, M. (2011). Andromeda: a peptide search engine integrated into the MaxQuant environment. *J. Proteome Res.* **10**, 1794–1805.
- Cristea, I.M., Williams, R., Chait, B.T., and Rout, M.P. (2005). Fluorescent proteins as proteomic probes. *Mol. Cell. Proteomics* **4**, 1933–1941.
- Davies, T.G., Wixted, W.E., Coyle, J.E., Griffiths-Jones, C., Hearn, K., McMenamin, R., Norton, D., Rich, S.J., Richardson, C., Saxty, G., et al. (2016). Monoacidic Inhibitors of the Kelch-like ECH-Associated Protein 1: Nuclear Factor Erythroid 2-Related Factor 2 (KEAP1:NRF2) Protein-Protein Interaction with High Cell Potency Identified by Fragment-Based Discovery. *J. Med. Chem.* **59**, 3991–4006.
- Dey, S., Sayers, C.M., Verginadis, I.I., Lehman, S.L., Cheng, Y., Cerniglia, G.J., Tuttle, S.W., Feldman, M.D., Zhang, P.J., Fuchs, S.Y., et al. (2015). ATF4-dependent induction of heme oxygenase 1 prevents anoikis and promotes metastasis. *J. Clin. Invest.* **125**, 2592–2608.
- Dimitrova, N., Gocheva, V., Bhutkar, A., Resnick, R., Jong, R.M., Miller, K.M., Bendor, J., and Jacks, T. (2016). Stromal Expression of miR-143/145 Promotes Neoangiogenesis in Lung Cancer Development. *Cancer Discov.* **6**, 188–201.
- Dobin, A., Davis, C.A., Schlesinger, F., Drenkow, J., Zaleski, C., Jha, S., Batut, P., Chaisson, M., and Gingeras, T.R. (2013). STAR: ultrafast universal RNA-seq aligner. *Bioinformatics* **29**, 15–21.
- Doi, K., Akaike, T., Fujii, S., Tanaka, S., Ikebe, N., Beppu, T., Shibahara, S., Ogawa, M., and Maeda, H. (1999). Induction of haem oxygenase-1 nitric oxide and ischaemia in experimental solid tumours and implications for tumour growth. *Br. J. Cancer* **80**, 1945–1954.
- DuPage, M., Dooley, A.L., and Jacks, T. (2009). Conditional mouse lung cancer models using adenoviral or lentiviral delivery of Cre recombinase. *Nat. Protoc.* **4**, 1064–1072.
- Fang, J., Sawa, T., Akaike, T., Akuta, T., Sahoo, S.K., Khaled, G., Hamada, A., and Maeda, H. (2003). In vivo antitumor activity of pegylated zinc protoporphyrin: targeted inhibition of heme oxygenase in solid tumor. *Cancer Res.* **63**, 3567–3574.
- Fellmann, C., Hoffmann, T., Sridhar, V., Hopfgartner, B., Muhar, M., Roth, M., Lai, D.Y., Barbosa, I.A., Kwon, J.S., Guan, Y., et al. (2013). An optimized microRNA backbone for effective single-copy RNAi. *Cell Rep.* **5**, 1704–1713.
- Goldstein, L.D., Lee, J., Gnad, F., Klijn, C., Schaub, A., Reeder, J., Daemen, A., Bakalarski, C.E., Holcomb, T., Shames, D.S., et al. (2016). Recurrent Loss of NFE2L2 Exon 2 Is a Mechanism for Nrf2 Pathway Activation in Human Cancers. *Cell Rep.* **16**, 2605–2617.
- Gozzelino, R., Jeney, V., and Soares, M.P. (2010). Mechanisms of cell protection by heme oxygenase-1. *Annu. Rev. Pharmacol. Toxicol.* **50**, 323–354.
- Hanada, N., Takahata, T., Zhou, Q., Ye, X., Sun, R., Itoh, J., Ishiguro, A., Kijima, H., Mimura, J., Itoh, K., et al. (2012). Methylation of the KEAP1 gene promoter region in human colorectal cancer. *BMC Cancer* **12**, 66.
- Hiramoto, K., Satoh, H., Suzuki, T., Moriguchi, T., Pi, J., Shimosegawa, T., and Yamamoto, M. (2014). Myeloid lineage-specific deletion of antioxidant system enhances tumor metastasis. *Cancer Prev. Res. (Phila.)* **7**, 835–844.
- Huttlin, E.L., Bruckner, R.J., Paulo, J.A., Cannon, J.R., Ting, L., Baltier, K., Colby, G., Gebreab, F., Gygi, M.P., Parzen, H., et al. (2017). Architecture of the human interactome defines protein communities and disease networks. *Nature* **545**, 505–509.
- Jaramillo, M.C., and Zhang, D.D. (2013). The emerging role of the Nrf2-Keap1 signaling pathway in cancer. *Genes Dev.* **27**, 2179–2191.
- Kinsella, R.J., Kähäri, A., Haider, S., Zamora, J., Proctor, G., Spudich, G., Almeida-King, J., Staines, D., Derwent, P., Kerhornou, A., et al. (2011). Ensembl BioMarts: a hub for data retrieval across taxonomic space. *Database (Oxford)* **2011**, bar030.
- Lee, U., Frankenberger, C., Yun, J., Bevilacqua, E., Caldas, C., Chin, S.F., Rueda, O.M., Reinitz, J., and Rosner, M.R. (2013). A prognostic gene signature for metastasis-free survival of triple negative breast cancer patients. *PLoS ONE* **8**, e82125.
- Li, C., and Stocker, R. (2009). Heme oxygenase and iron: from bacteria to humans. *Redox Rep.* **14**, 95–101.
- Liang, Y., Wu, H., Lei, R., Chong, R.A., Wei, Y., Lu, X., Tagkopoulos, I., Kung, S.Y., Yang, Q., Hu, G., and Kang, Y. (2012). Transcriptional network analysis identifies BACH1 as a master regulator of breast cancer bone metastasis. *J. Biol. Chem.* **287**, 33533–33544.
- Liberzon, A., Subramanian, A., Pinchback, R., Thorvaldsdóttir, H., Tamayo, P., and Mesirov, J.P. (2011). Molecular signatures database (MSigDB) 3.0. *Bioinformatics* **27**, 1739–1740.
- Love, M.I., Huber, W., and Anders, S. (2014). Moderated estimation of fold change and dispersion for RNA-seq data with DESeq2. *Genome Biol.* **15**, 550.
- Malhotra, D., Portales-Casamar, E., Singh, A., Srivastava, S., Arenillas, D., Happel, C., Shyr, C., Wakabayashi, N., Kensler, T.W., Wasserman, W.W., and Biswal, S. (2010). Global mapping of binding sites for Nrf2 identifies novel targets in cell survival response through ChIP-Seq profiling and network analysis. *Nucleic Acids Res.* **38**, 5718–5734.
- Mena, E.L., Kjolby, R.A.S., Saxton, R.A., Werner, A., Lew, B.G., Boyle, J.M., Harland, R., and Rape, M. (2018). Dimerization quality control ensures neuronal development and survival. *Science* **362**, eaap8236.
- Mense, S.M., and Zhang, L. (2006). Heme: a versatile signaling molecule controlling the activities of diverse regulators ranging from transcription factors to MAP kinases. *Cell Res.* **16**, 681–692.
- Mootha, V.K., Lindgren, C.M., Eriksson, K.F., Subramanian, A., Sihag, S., Lehar, J., Puigserver, P., Carlsson, E., Ridderstråle, M., Laurila, E., et al. (2003). PGC-1 α -responsive genes involved in oxidative phosphorylation are coordinately downregulated in human diabetes. *Nat. Genet.* **34**, 267–273.
- Morita, T., Perrella, M.A., Lee, M.E., and Kourembanas, S. (1995). Smooth muscle cell-derived carbon monoxide is a regulator of vascular cGMP. *Proc. Natl. Acad. Sci. USA* **92**, 1475–1479.
- Muscarella, L.A., Barbano, R., D'Angelo, V., Copetti, M., Coco, M., Balsamo, T., la Torre, A., Notarangelo, A., Troiano, M., Parisi, S., et al. (2011). Regulation of KEAP1 expression by promoter methylation in malignant gliomas and association with patient's outcome. *Epigenetics* **6**, 317–325.
- Ogawa, K., Sun, J., Taketani, S., Nakajima, O., Nishitani, C., Sassa, S., Hayaishi, N., Yamamoto, M., Shibahara, S., Fujita, H., and Igarashi, K. (2001). Heme mediates derepression of Maf recognition element through direct binding to transcription repressor Bach1. *EMBO J.* **20**, 2835–2843.
- Orthwein, A., Noordermeer, S.M., Wilson, M.D., Landry, S., Enchev, R.I., Sherker, A., Munro, M., Pinder, J., Salsman, J., Dellaire, G., et al. (2015). A mechanism for the suppression of homologous recombination in G1 cells. *Nature* **528**, 422–426.
- Oyake, T., Itoh, K., Motohashi, H., Hayashi, N., Hoshino, H., Nishizawa, M., Yamamoto, M., and Igarashi, K. (1996). Bach proteins belong to a novel family of BTB-basic leucine zipper transcription factors that interact with MafK and regulate transcription through the NF-E2 site. *Mol. Cell. Biol.* **16**, 6083–6095.
- Pagan, J.K., Marzio, A., Jones, M.J., Saraf, A., Jallepalli, P.V., Florens, L., Washburn, M.P., and Pagano, M. (2015). Degradation of Cep68 and PCNT cleavage mediate Cep215 removal from the PCM to allow centriole separation, disengagement and licensing. *Nat. Cell Biol.* **17**, 31–43.
- Pamplona, A., Ferreira, A., Balla, J., Jeney, V., Balla, G., Epiphany, S., Chora, A., Rodrigues, C.D., Gregoire, I.P., Cunha-Rodrigues, M., et al. (2007). Heme oxygenase-1 and carbon monoxide suppress the pathogenesis of experimental cerebral malaria. *Nat. Med.* **13**, 703–710.
- Ran, F.A., Hsu, P.D., Wright, J., Agarwala, V., Scott, D.A., and Zhang, F. (2013). Genome engineering using the CRISPR-Cas9 system. *Nat. Protoc.* **8**, 2281–2308.
- Reichard, J.F., Motz, G.T., and Puga, A. (2007). Heme oxygenase-1 induction by NRF2 requires inactivation of the transcriptional repressor BACH1. *Nucleic Acids Res.* **35**, 7074–7086.

- Rojo de la Vega, M., Chapman, E., and Zhang, D.D. (2018). NRF2 and the Hallmarks of Cancer. *Cancer Cell* 34, 21–43.
- Romero, R., Sayin, V.I., Davidson, S.M., Bauer, M.R., Singh, S.X., LeBoeuf, S.E., Karakousi, T.R., Ellis, D.C., Bhutkar, A., Sánchez-Rivera, F.J., et al. (2017). Keap1 loss promotes Kras-driven lung cancer and results in dependence on glutaminolysis. *Nat. Med.* 23, 1362–1368.
- Sánchez-Rivera, F.J., Papagiannakopoulos, T., Romero, R., Tammela, T., Bauer, M.R., Bhutkar, A., Joshi, N.S., Subbaraj, L., Bronson, R.T., Xue, W., and Jacks, T. (2014). Rapid modelling of cooperating genetic events in cancer through somatic genome editing. *Nature* 516, 428–431.
- Sayin, V.I., LeBoeuf, S.E., Singh, S.X., Davidson, S.M., Biancur, D., Guzelhan, B.S., Alvarez, S.W., Wu, W.L., Karakousi, T.R., Zavitsanou, A.M., et al. (2017). Activation of the NRF2 antioxidant program generates an imbalance in central carbon metabolism in cancer. *eLife* 6, e28083.
- Shang, F.T., Hui, L.L., An, X.S., Zhang, X.C., Guo, S.G., and Kui, Z. (2015). ZnPPIX inhibits peritoneal metastasis of gastric cancer via its antiangiogenic activity. *Biomed. Pharmacother.* 71, 240–246.
- Smith, C.L., Blake, J.A., Kadin, J.A., Richardson, J.E., and Bult, C.J.; Mouse Genome Database Group (2018). Mouse Genome Database (MGD)-2018: knowledgebase for the laboratory mouse. *Nucleic Acids Res.* 46 (D1), D836–D842.
- Subramanian, A., Tamayo, P., Mootha, V.K., Mukherjee, S., Ebert, B.L., Gillette, M.A., Paulovich, A., Pomeroy, S.L., Golub, T.R., Lander, E.S., and Mesirov, J.P. (2005). Gene set enrichment analysis: a knowledge-based approach for interpreting genome-wide expression profiles. *Proc. Natl. Acad. Sci. USA* 102, 15545–15550.
- Sun, J., Hoshino, H., Takaku, K., Nakajima, O., Muto, A., Suzuki, H., Tashiro, S., Takahashi, S., Shibahara, S., Alam, J., et al. (2002). Hemoprotein Bach1 regulates enhancer availability of heme oxygenase-1 gene. *EMBO J.* 21, 5216–5224.
- Sun, J., Brand, M., Zenke, Y., Tashiro, S., Groudine, M., and Igarashi, K. (2004). Heme regulates the dynamic exchange of Bach1 and NF-E2-related factors in the Maf transcription factor network. *Proc. Natl. Acad. Sci. USA* 101, 1461–1466.
- Sunamura, M., Duda, D.G., Ghattas, M.H., Lozonschi, L., Motoi, F., Yamauchi, J., Matsuno, S., Shibahara, S., and Abraham, N.G. (2003). Heme oxygenase-1 accelerates tumor angiogenesis of human pancreatic cancer. *Angiogenesis* 6, 15–24.
- Suzuki, T., and Yamamoto, M. (2015). Molecular basis of the Keap1-Nrf2 system. *Free Radic. Biol. Med.* 88 (Pt B), 93–100.
- Tan, M.K., Lim, H.J., Bennett, E.J., Shi, Y., and Harper, J.W. (2013). Parallel SCF adaptor capture proteomics reveals a role for SCFFBXL17 in NRF2 activation via BACH1 repressor turnover. *Mol. Cell* 52, 9–24.
- Tanaka, S., Akaike, T., Fang, J., Beppu, T., Ogawa, M., Tamura, F., Miyamoto, Y., and Maeda, H. (2003). Antiapoptotic effect of haem oxygenase-1 induced by nitric oxide in experimental solid tumour. *Br. J. Cancer* 88, 902–909.
- Tebay, L.E., Robertson, H., Durant, S.T., Vitale, S.R., Penning, T.M., Dinkova-Kostova, A.T., and Hayes, J.D. (2015). Mechanisms of activation of the transcription factor Nrf2 by redox stressors, nutrient cues, and energy status and the pathways through which it attenuates degenerative disease. *Free Radic. Biol. Med.* 88 (Pt B), 108–146.
- The UniProt Consortium (2017). UniProt: the universal protein knowledgebase. *Nucleic Acids Res.* 45 (D1), D158–D169.
- Thompson, A., Schäfer, J., Kuhn, K., Kienle, S., Schwarz, J., Schmidt, G., Neumann, T., Johnstone, R., Mohammed, A.K., and Hamon, C. (2003). Tandem mass tags: a novel quantification strategy for comparative analysis of complex protein mixtures by MS/MS. *Anal. Chem.* 75, 1895–1904.
- Wang, H., Liu, X., Long, M., Huang, Y., Zhang, L., Zhang, R., Zheng, Y., Liao, X., Wang, Y., Liao, Q., et al. (2016). NRF2 activation by antioxidant antidiabetic agents accelerates tumor metastasis. *Sci. Transl. Med.* 8, 334ra351.
- Warnatz, H.J., Schmidt, D., Manke, T., Piccini, I., Sultan, M., Borodina, T., Balzereit, D., Wruck, W., Soldatov, A., Vingron, M., et al. (2011). The BTB and CNC homology 1 (BACH1) target genes are involved in the oxidative stress response and in control of the cell cycle. *J. Biol. Chem.* 286, 23521–23532.
- Was, H., Cichon, T., Smolarczyk, R., Rudnicka, D., Stopa, M., Chevalier, C., Leger, J.J., Lackowska, B., Grochot, A., Bojkowska, K., et al. (2006). Overexpression of heme oxygenase-1 in murine melanoma: increased proliferation and viability of tumor cells, decreased survival of mice. *Am. J. Pathol.* 169, 2181–2198.
- Wiel, C., Le Gal, K., Ibrahim, M.X., Jahangir, C.A., Kashif, M., Ziegler, D.V., Xu, X., Ghosh, T., Mondal, T., Kanduri, C., et al. (2019). BACH1 Stabilization by Antioxidants Stimulates Lung Cancer Metastasis. *Cell* 178, this issue, 330–345.
- Winslow, M.M., Dayton, T.L., Verhaak, R.G., Kim-Kiselak, C., Snyder, E.L., Feldser, D.M., Hubbard, D.D., DuPage, M.J., Whittaker, C.A., Hoersch, S., et al. (2011). Suppression of lung adenocarcinoma progression by Nkx2-1. *Nature* 473, 101–104.
- Yun, J., Frankenberger, C.A., Kuo, W.L., Boelens, M.C., Eves, E.M., Cheng, N., Liang, H., Li, W.H., Ishwaran, H., Minn, A.J., and Rosner, M.R. (2011). Signaling pathway for RKIP and Let-7 regulates and predicts metastatic breast cancer. *EMBO J.* 30, 4500–4514.
- Zenke-Kawasaki, Y., Dohi, Y., Katoh, Y., Ikura, T., Ikura, M., Asahara, T., Tokunaga, F., Iwai, K., and Igarashi, K. (2007). Heme induces ubiquitination and degradation of the transcription factor Bach1. *Mol. Cell. Biol.* 27, 6962–6971.
- Zerbino, D.R., Achuthan, P., Akanni, W., Amode, M.R., Barrell, D., Bhai, J., Billis, K., Cummins, C., Gall, A., Girón, C.G., et al. (2018). Ensembl 2018. *Nucleic Acids Res.* 46 (D1), D754–D761.
- Zhang, L., Wang, N., Zhou, S., Ye, W., Jing, G., and Zhang, M. (2012). Propofol induces proliferation and invasion of gallbladder cancer cells through activation of Nrf2. *J. Exp. Clin. Cancer Res.* 31, 66.
- Zhang, M., Zhang, C., Zhang, L., Yang, Q., Zhou, S., Wen, Q., and Wang, J. (2015). Nrf2 is a potential prognostic marker and promotes proliferation and invasion in human hepatocellular carcinoma. *BMC Cancer* 15, 531.
- Zheng, G., Ma, Y., Zou, Y., Yin, A., Li, W., and Dong, D. (2018). HCCMDB: the human cancer metastasis database. *Nucleic Acids Res.* 46 (D1), D950–D955.

STAR★METHODS

KEY RESOURCES TABLE

REAGENT or RESOURCE	SOURCE	IDENTIFIER
Antibodies		
Bach1 (WB = 1:1000, IHC = 1:500)	Bethyl	Cat#A303-058A; RRID: AB_10894145
Ho1 (WB = 1:1000, IHC = 1:100)	Bethyl	Cat#A303-662A; RRID: AB_11205464
Bach1 (1:1000)	R&D Systems	Cat#AF5776; RRID: AB_2061974
Bach1 (1:100)	R&D Systems	Cat#AF5777; RRID: AB_2061817
Skp1 (1:5000)	Michele Pagano's lab	N/A
Fbxo22 (WB = 1:1000, IHC = 1:100)	Proteintech	Cat#13606-1-AP; RRID: AB_2104403
Fbxo22 (1:1000)	GeneTex	Cat#GTX117774; RRID: AB_10619633
Nrf2 (1:1000)	Cell Signaling	Cat#12721S; RRID: AB_2715528
Keap1 (1:10000)	Proteintech	Cat#10503-2-AP; RRID: AB_2132625
Palb2 (1:1000)	Bethyl	Cat#A301-247A; RRID: AB_890608
alpha-Tubulin (1:10000)	Sigma-Aldrich	Cat#T6074-200UL; RRID: AB_477582
Cul1 (1:1000)	Thermo Fisher Scientific	Cat#718700; RRID: AB_2534002
HA (1:1000)	Sigma-Aldrich	Cat#H3663; RRID: AB_262051
Flag (1:4000)	Sigma-Aldrich	Cat#F1804; RRID: AB_262044
Biological Samples		
Human Tissue Microarray	US Biomax	LC817a
Primary human LUAD	NYU Center for Biospecimen Research and Development	N/A
Patient Derived Xenografts	Papagiannakopoulos and Rudin Laboratories	Romero et al., 2017
Chemicals, Peptides, and Recombinant Proteins		
Cycloheximide (100 µg/mL)	Sigma-Aldrich	Cat#C7698-1G
Doxycycline	Sigma-Aldrich	Cat#D9891
Lipofectamine 3000	Thermo Fisher Scientific	Cat#L3000150
MG132 (10 µM)	Peptides International	Cat#IZL-3175v
MLN4924 (2 µM)	Active Biochem	Cat#A-1139
Polybrene (8 mg/mL)	Sigma-Aldrich	Cat#TR-1003
Puromycin	Sigma-Aldrich	Cat#P9620
RNAi Max (Lipofectamine)	Thermo Fisher Scientific	Cat#13778-500
Hemin (10 µM)	Sigma-Aldrich	Cat#51280-1G
Tin protoporphyrin IX vdichloride (10 µM)	Tocris	Cat#0747
Zinc Protoporphyrin-9 (40 mg/kg)	Cayman Chemical	Cat#14483
Ki696 (1 µM)	Craig Thomas's lab	N/A
Poly(ethylene glycol)	Sigma-Aldrich	Cat#202371
Deposited data		
RNA sequencing data	This study	GEO: GSE122836
Proteomic data	This study	MassIVE ID: MSV000083157 and ProteomeXchange ID: PXD011818.
Original images of western blot data	This study; Mendeley Data This study; Mendeley Data	https://data.mendeley.com/datasets/m6vrdbwsnc/draft?a=42056e38-861b-41f1-a5c6-0fb9263327ff
Experimental Models: Cell Lines		
A549	ATCC	Cat#CCL-185; RRID: CVCL_0023
H2009	ATCC	Cat#CRL-5911; RRID: CVCL_1514

(Continued on next page)

Continued		
REAGENT or RESOURCE	SOURCE	IDENTIFIER
HEK293T	ATCC	Cat#CRL-3216; RRID: CVCL_0063
KP cells (Kras ^{G12D/+} ; p53 ^{-/-})	Papagiannakopoulos Laboratory	Romero et al., 2017
KPK cells (Kras ^{G12D/+} ; p53 ^{-/-} ; Keap1 ^{-/-})	Papagiannakopoulos Laboratory	Romero et al., 2017
Experimental Models: Organisms/Strains		
NCr Nude mice (CrTac:NCr-Foxn1 ^{nu})	Taconic	NCRNU-M, https://www.taconic.com/mouse-model/ncr-nude
C57BL/6J	Jackson Laboratory	000664, https://www.jax.org/strain/000664
Kras ^{G12D/+} ; p53 ^{-/-} , mixed C57BL/6J and 129S1/SvImJ	Papagiannakopoulos Laboratory	N/A
Kras ^{G12D/+} ; p53 ^{-/-} ; Rosa26 ^{LSL-Cas9-2a-GFP} , mixed C57BL/6J and 129S1/SvImJ	Papagiannakopoulos Laboratory and Jackson Laboratory	Rosa26LSL-Cas9-2a-GFP: 024857, https://www.jax.org/strain/024857
Oligonucleotides		
Full list of oligos	See Table S7	N/A
Recombinant DNA		
pcDNA3.1 2xFLAG-2xSTREP-Bach1	Michele Pagano's lab	N/A
pcDNA3.1 2xFLAG-2xSTREP-Fbxo22	Michele Pagano's lab	N/A
pcDNA3.1 2xFLAG-2xSTREP-Keap1	Michele Pagano's lab	N/A
Software and Algorithms		
ImageJ software 2.0.	ImageJ software	https://imagej.net/ImageJ2
GraphPad- Prism 7.0e	GraphPad Software	https://www.graphpad.com/scientific-software/prism/
ICM 3.8-4a	Molsoft LLC	http://www.mybiosoftware.com/

LEAD CONTACT AND MATERIALS AVAILABILITY

Further information and requests for resources and reagents should be directed to and will be fulfilled by the Lead Contact, Michele Pagano (michele.pagano@nyumc.org).

EXPERIMENTAL MODEL AND SUBJECT DETAILS

Animal experiments

All animal studies described were approved by the NYU Langone Medical Center Institutional Animal Care and Use Committee. 2.5×10^5 cells were implanted subcutaneously into 5-8 week old male nude mice (Foxn1nu). After tumor establishment phase, approximately 10 days post implantation (tumors 100-150mm³), all animals were put on a doxycycline diet (200mg/kg), 4 days after, at day 14, mice were randomized and assigned to groups: vehicle or ZnPIX treatment. Animals were treated with 40 mg/kg ZnPIX (Cayman Chemical) or vehicle once a day administered through intraperitoneal injection. The drug and vehicle containing 4% DMSO 30% polyethylene glycol (PEG) and 66% saline was formulated daily. LSL-KrasG12D; Trp53flox mice have already been described (DuPage et al., 2009). For all mouse studies, > 3 mice were used for each experimental cohort per specified genotype. All mice were maintained on a mixed genetic background containing C57BL/6- 129/Sv. Mice with the appropriate genotype were randomly selected to begin tumor initiation studies with pSECC-sgTom or pSECC-sgKeap1, and uSEC-sgTom, uSEC-sgKeap1 or uSEC-sgFbxo22. Mice were infected intratracheally with lentiviruses as described (DuPage et al., 2009). The total lung area occupied by each tumor was measured on H&E-stained slides using NISElements software (Nikon) or Biopix IQ. All tumor burden and IHC analyses were done in a blinded fashion, in which the researcher was unaware of which genotype of the samples. For allograft experiments, cells derived from mouse lung tumors were transplanted subcutaneously (2.5×10^5 cells) under the skin or orthotopically (5×10^4 cells) in the lungs of 5-8 week old male nude (Foxn1nu) or 5-8 week old female C57BL/6J mice. Subcutaneous tumor volumes were calculated according to the following formula ($a \times b^2$)/2.

Cell Culture Procedures

Parental cell lines from KP mice were previously established and described (Dimitrova et al., 2016). HEK293T (female), A549 (male), H2009 (female), cell lines were propagated in DMEM at 37°Celsius. All media were supplemented with 10% fetal bovine

serum (FBS) (Corning Life Sciences) and 1% penicillin/streptomycin/L-glutamine (Corning Life Sciences). For A549 or H2009 cells stably infected with pTRIPZ vectors, KP cells stably infected with pTRIPZ and pLVX-mCherry vectors, and A549 or KP or KPK infected with mirE vectors, cells were propagated in DMEM supplemented with 10% Tet system-approved FBS (Takara/Clontech Laboratories) and 1% penicillin/streptomycin/L-glutamine (Corning Life Sciences). Doxycycline (Sigma-Aldrich) was used at 0.1 $\mu\text{g}/\text{mL}$, Cycloheximide (Sigma-Aldrich) at 100 $\mu\text{g}/\text{mL}$, MLN4924 (Active Biochem) at 2 μM , MG132 (Peptides International) at 10 μM , Hemin (Sigma-Aldrich) at 10 μM , Tin protoporphyrin IX dichloride (TinPPIX) (Tocris) at 10 μM , Ki696 (provided by Craig Thomas lab) at 1 μM . DMSO was used as vehicle treatment in both transwell and scratch assay. Cells were periodically screened for *Mycoplasma* contamination. No cell lines used in this study were found in the database of commonly misidentified cell lines that is maintained by ICLAC and NCBI Biosample. Specific details about cell lines used are provided in the [Key Resources Table](#).

Human lung cancer with matched lymph node metastasis tissue array, human clinical lung cancer samples and Patient derived xenografts (PDXs)

Lung carcinoma with matched lymph node metastasis tissue microarray (US biomax, Inc. cat. No. LC817a), and clinical lung cancer samples from NYU biospecimen core and PDX materials that were *KEAP1* mutant or *KEAP1* wild-type [both previously described and generated ([Romero et al., 2017](#))] were probed with antibodies against Bach1 (Bethyl Laboratories, A303-058A) and Ho1 (Bethyl Laboratories, A303-662A). Immunocytochemistry was performed in a Leica Bond Max (Leica Biosystem).

METHOD DETAILS

CRISPR genome editing

Generation of KP, KPK, KP-*Nrf2* KO cells were previously generated and described ([Romero et al., 2017](#)). To generate *Fbxo22*, *Bach1* and *Ho1* knockout KP cells, optimal sgRNA target sequences closest to the genomic target sites were designed using the Benchling CRISPR Genome Engineering tool. *Fbxo22*, *Bach1* and *Ho1* sgRNA target sequences (see [Table S7](#)) were cloned into pSpCas9(BB)-2A-GFP (PX458), a gift from F. Zhang (Addgene plasmid no. 48138) ([Ran et al., 2013](#)). KP cells were seeded into 10 cm dishes at a 70% confluency, and transfected with 5 μg of the appropriate sgRNA-containing PX458 plasmid, using Lipofectamine 3000 (Life Technologies). The transfection was performed according to the manufacturer's recommended protocol, using a 2:1 ratio of Lipofectamine/DNA. Two days after transfection, GFP-positive cells were sorted using the Beckman Coulter MoFlo XDP cell sorter (100 m nozzle), and 15,000 cells were plated on a 15 cm dish. Eight to ten days later, single KP clones were picked, trypsinized in 0.25% trypsin EDTA for 5 min, and plated into individual wells of a 96-well plate for genotyping. Genomic DNA was collected using QuickExtract (Epicenter). Genotyping PCRs were performed with MangoTaq DNA Polymerase (Bioline), using primers surrounding the genomic target site. The resulting PCR products were purified and sequenced to determine the presence of an insertion or deletion event. To further validate the mutational status of candidate clones, the PCR products were subjected to TOPO-TA Cloning (Invitrogen), and sequenced to distinguish the amplified products of distinct alleles. Fifty bacterial colonies for each TOPO-TA cloning reaction were sequenced and aligned to the corresponding wild-type template in Benchling. Clones positive to insertion or deletion events were validated also by western blot.

Gene Set Enrichment Analysis

Gene set Enrichment Analysis (GSEA) ([Mootha et al., 2003](#); [Subramanian et al., 2005](#)) (which ultimately relies on gene-sets of human origin), was performed using the mouse transcriptomics data after projection to the assigned human orthologs (as described below in the Transcriptomics Data Analysis section). The analysis was performed using java GSEA Desktop Application with default parameters and considered two gene-sets: (1) the C3:TFT gene-set which is provided as part of MSigDB V6.2 ([Liberzon et al., 2011](#)) and contains target gene-sets for a series of human transcription factors and putative motifs, (2) a database of genes generated by extraction of all genes reported by Human Cancer Metastasis Database (HCMDDB) ([Zheng et al., 2018](#)) ([Figure 1E](#)). In [Figure S6A](#) we employed an integrated Bach1 gene set that we generated by combining the Bach1 MSigDB signature with a Bach1 target gene list obtained from ChIP-Seq data previously published ([Warnatz et al., 2011](#)).

Gene Silencing by siRNA

The following siRNA (GE Healthcare) were used: ON-TARGETplus siRNA oligos targeting human and mouse *Fbxo22* (see [Table S7](#)). The first two efficient siRNAs, along with a non-targeting siRNA as control, were used in the study: #1 and #2 for human; #2 and #4 for mouse. All siRNA were transfected into different cell lines using RNAi Max (Thermo Fisher Scientific). ON-TARGETplus non-targeting siRNA #1 (GE Healthcare, catalog no. D-001810-01) served as a negative control.

Human clinical data analyses

Genomic data for samples from subjects with lung adenocarcinoma ($n = 576$) were obtained from TCGA LUAD (<https://www.cancer.gov/about-nci/organization/ccg/research/structural-genomics/tcga>). This included RNA-seq gene expression profiles of primary tumor samples from subjects ($n = 515$) and associated clinical data ($n = 515$ subjects with RNA-seq data for primary

tumors with associated survival data). Individual sample expression profiles were scored against the MSigDB (<http://software.broadinstitute.org/gsea/msigdb>) Bach1 signature (BACH1_01) using ssGSEA (Barbie et al., 2009; Subramanian et al., 2005). Patients were stratified according to their correlation score with the Bach1 signature and Kaplan–Meier survival analyses were conducted between the top 20% of correlated patients versus the rest of the LUAD cohort. The log-rank test was used to assess significance. Additionally, the Cox proportional hazards regression model was used to analyze the prognostic value of the Bach1 signature across all subjects within the TCGA LUAD cohort in the context of additional clinical covariates. All univariate and multivariable analyses were conducted within a 5-year survival time frame. The following subject and tumor-stage clinical characteristics were used: signature (Bach1 signature strong versus weak correlation); gender (male versus female); age (years, continuous); smoking history (reformed > 15 y versus nonsmoker, reformed < 15 y versus nonsmoker, current smoker versus nonsmoker); Union for International Cancer Control (UICC) tumor nodes metastasis (TNM) stage specification (stage III or IV versus I or II); UICC T-score specification (T3 or T4 versus T1 or T2); UICC N-score specification (N1 or N2 versus N0); Tumor purity (Fraction cancer nuclei from Campbell et al. [2016] using ABSOLUTE [Carter et al., 2012]). Hazard ratio proportionality assumptions for the Cox regression model were validated by testing for all interactions simultaneously ($p = 0.773$). Interaction between the Bach1 signature and T score, N score, and Tumor purity (significant covariates in the model) were tested using a likelihood-ratio test (LRT) to contrast a model consisting of both covariates with another model consisting of both covariates plus an interaction term. No statistically significant difference was found between the two models (T score: $p = 0.893$; N score: $p = 0.909$; Tumor purity $p = 0.705$; likelihood-ratio test). To test for statistically significant association between Bach1 signature correlation scores and TCGA LUAD TNM stage (stages I–IV), T-scores, and N-scores, the Kurskal–Wallis test was used to assess overall significance, and the Kolmogorov–Smirnov test was used to assess pairwise differences. An analysis pipeline configured using a previously released TCGA dataset with 488 primary tumor samples and associated clinical data was utilized. Results were visualized using empirical cumulative distribution function (ECDF) plots. All statistical analyses were conducted in R (<http://www.R-project.org>), and all survival analyses were conducted using the survival package in R.

Immunoprecipitation and immunoblotting

HEK293T cells were transiently transfected using polyethylenimine. Where indicated, 24 hours after transfection, HEK293T cells were incubated with MLN4924 for 3 hours before collection. Cell lysis was carried out with lysis buffer (50 mM Tris pH 8.0, 150 mM NaCl, 10% glycerol, 1 mM EDTA, 50 mM NaF, and 0.1% NP-40) supplemented with protease and phosphatase inhibitors. Lysates were then immunoprecipitated with anti-FLAG antibody conjugated to agarose. Elution of the immunoprecipitate for anti-FLAG agarose resin was carried out with FLAG peptide. For immunoprecipitation of endogenous proteins, HEK293T cells were collected and lysed with lysis buffer. Bach1 was immunoprecipitated with the listed antibody mixed with Dynabeads Protein G (Thermo Fisher Scientific). Rabbit IgG (Bethyl) was used as a negative control. Elution of the immunoprecipitate was carried out with NuPAGE® LDS sample buffer (Thermo Fisher Scientific) supplemented with β -mercaptoethanol (Sigma-Aldrich) and incubation at 95°C for 5 minutes. Immunoblotting was performed as previously described (Pagan et al., 2015). Briefly, samples were resolved under denaturing and reducing conditions using 4%–12% Bis-Tris gels (NuPAGE®) and transferred to a PDVF membrane (Immobilon-P, Millipore). Membranes were blocked with 5% nonfat dried milk, incubated with primary antibodies overnight at 4°C. After washing the membranes, secondary antibodies coupled with horseradish peroxidase were applied (Amersham-GE). Immunoreactive bands were visualized by enhanced chemiluminescence reagent (Thermo Fisher Scientific).

Immunohistochemistry and immunofluorescence

Mice were euthanized by carbon dioxide asphyxiation. Lungs were perfused through the trachea with 10% neutral buffered formalin, fixed overnight, transferred to 70% ethanol, and subsequently embedded in paraffin. Sections were cut at a thickness of 3 μ m and stained with H&E for pathological examination. Chromogenic IHC was performed on a Ventana Medical Systems DISCOVERY XT instrument with online deparaffinization using Ventana's reagents and detection kits and antigen retrieved in Ventana Cell Conditioner 1 or 2. The following antibodies were used for IHC: anti-Bach1 (Bethyl, A303-058 1:500), anti-Bach1 (R&D Systems, AF5777 1:100), anti-Ho1 (Bethyl, A303-662A 1:100), anti-Fbxo22 (Proteintech, 13606-1-AP 1:100). HRP detection was used for Ho1, Bach1, Fbxo22. Antigen retrieval was performed in a Ventana Cell Conditioner 1 (TBE). Pictures were obtained using a Nikon 80i microscope with a DS-U3 camera and NIS-Elements software and with a digital whole-slide scanner (Leica, SCN400F) and Slidepath software version 4.0.8.

Lentivirus-Mediated gene transfer

HEK293T were transiently co-transfected with lentiviral (pTRIPZ and pLVX-mCherry) vectors containing vesicular stomatitis virus G protein (VSV-G) and the gene of interest along with pCMV Delta R8.2 using polyethylenimine. Lentivirus-containing medium, 48 hr after transfection, was collected and supplemented with 8 mg ml⁻¹ Polybrene (Sigma). KP, A549 and H2009 cells were infected by replacing the cell culture medium with the viral supernatant for 6 hours. Selection of stable clones was carried out using puromycin for pTRIPZ and mCherry for pLVX.

Mass Spectrometry

Preparation of Affinity Purification Samples for Mass Spectrometry. Samples and empty vector control were resuspended in NuPAGE® LDS Sample Buffer (Novex). The samples were reduced with 2 μ L of 0.2M dithiothreitol (Sigma) for one hour at 57°C at pH 8.0 and subsequently alkylated with 2 μ L of 0.5M iodoacetamide (Sigma) for 45 minutes at room temperature in the dark. The samples were loaded immediately onto a NuPAGE® 4%–12% Bis-Tris Gel 1.0 mm (Life Technologies) and run at 200V. The gel was stained with GelCode Blue Stain Reagent (Thermo). The gel plugs were excised and destained in a 1:1 (v/v) solution of methanol and 100mM ammonium bicarbonate. The gel plugs were incubated with 250ng of sequencing grade modified trypsin (Promega) in 100mM ammonium bicarbonate. The gel plugs digested overnight with gentle agitation. The digestion was halted by adding a slurry of R2 50 μ m Poros beads (Applied Biosystems) in 5% formic acid and 0.2% trifluoroacetic acid (TFA) to each sample (Cristea et al., 2005). The samples were allowed to shake at 4°C for 2 hours. The beads were loaded onto C18 ziptips (Millipore), equilibrated with 0.1% TFA. The beads were washed with 0.5% acetic acid. Peptides were eluted with 40% acetonitrile in 0.5% acetic acid followed by 80% acetonitrile in 0.5% acetic acid. The organic solvent was removed using a SpeedVac concentrator and the sample reconstituted in 0.5% acetic acid.

Mass Spectrometry Analysis Affinity Purification. An aliquot of each sample was loaded onto an Acclaim PepMap trap column (75 μ m ID x 2cm, 3 μ m bead size, 100Å pore size) in line with an EASY-Spray PepMap analytical column (75 μ m ID x 50cm C18, 2 μ m bead size, 100Å pore size) using the auto sampler of an EASY-nLC 1000 HPLC (ThermoFisher) and solvent A (2% acetonitrile, 0.5% acetic acid). The peptides were eluted into a ThermoFisher Scientific Orbitrap Fusion Lumos Mass Spectrometer increasing from 5% to 35% solvent B (80% acetonitrile, 0.5% acetic acid) over 60 minutes, followed by an increase from 35% to 45% solvent B over 15 minutes followed by an increase of 45 to 100% solvent B in 10 min.

High resolution full MS spectra were obtained with a resolution of 120,000, an AGC target of 4e5, with a maximum ion time of 50ms, and a scan range from 400 to 1500 m/z. Following each full MS scan, low resolution MS/MS spectra were acquired for a 3 s duty cycle. The MS/MS spectra were collected in the ion trap in rapid scan mode, with an AGC target of 1e5, maximum ion time of 30ms, one microscan, 2 m/z isolation window, Normalized Collision Energy (NCE) of 32 and a dynamic exclusion of 30 msec.

Data Analysis. All acquired MS2 spectra were searched against a UniProt human database using Sequest within Proteome Discoverer (Thermo Scientific). The search parameters were as follows: precursor mass tolerance \pm 10 ppm, fragment mass tolerance \pm 0.4 Da, digestion parameters allowing trypsin 2 missed cleavages, fixed modification of carbamidomethyl on cysteine, variable modification of oxidation on methionine, and variable modification of deamidation on glutamine and asparagine. Peptides were filtered to better than 1% FDR using a target-decoy database strategy and proteins require at least two unique peptides to be reported.

Sample preparation for multiplexed quantitation. 500 μ g of each protein lysates (obtained using a buffer: 20 mM HEPES pH 8.0, 8 M urea) were reduced using dithiothreitol (5 μ L of 0.2 M) for 1 h at 55°C. The reduced cysteines were subsequently alkylated with iodoacetamide (5 μ L of 0.5 M) for 45 min in the dark at room temperature. The samples were digested with LysC at a 200:1 (protein:enzyme) ratio for 2 hours at 37°C. Next, 100 mM ammonium bicarbonate (pH 8.0) was added to dilute the urea concentration to 2 M and the protein lysates were digested with trypsin (Promega) at a 100:1 (protein:enzyme) ratio overnight at room temperature. The digested protein lysates was acidified to pH < 3 using trifluoroacetic acid (TFA) and desalted using C18 solid-phase extraction (Sep-Pak, Waters). The desalted peptides were eluted using first 40% acetonitrile (ACN) in 0.5% acetic acid followed by 80% acetonitrile (ACN) in 0.5% acetic acid. The peptide eluate was concentrated using the SpeedVac and stored at -80° C.

Plasmids

Bach1, Fbxo22 and Keap1 complementary cDNAs were inserted into a variety of vectors (modified pcDNA3.1 vectors containing N-terminal FLAG and STREP tags; pTRIPZ-puromycin lentiviral vector containing N-terminal FLAG and STREP tags; pLVX-mCherry lentiviral vector) by sub-cloning or site-directed mutagenesis (KAPA Biosystems). Specific details will be provided on request.

Proteomics Data Analysis

The first majority protein in each ProteinGroup of the MaxQuant (Cox and Mann, 2008) report was mapped to an MGI mouse gene accession using UniProt's (The UniProt Consortium, 2017) mapping (ftp://ftp.uniprot.org/pub/databases/uniprot/current_release/knowledgebase/idmapping/by_organism/MOUSE_10090_idmapping.dat.gz, downloaded on August, 2018) such that each MGI mouse gene is represented by a single ProteinGroup. This mapping was further leveraged to select a human ortholog (as was done with the transcriptomics data) such that every ProteinGroup maps to a single human ortholog. Many-to-one mappings between mouse and human genes were eliminated by selecting the candidate mouse ProteinGroup with the maximal signal intensity across all samples.

Scratch Assay

We utilized a scratch assay to measure the cell migration. 6×10^5 cells were seeded in each well of a 24 multiwell dish (Corning, Cat. no. 353047). After 24 hours, the cell layer was scratched by a 1000 μ L pipette tip, plates were incubated at 37°C, 5% CO₂, in a Cytation 5 Cell Imaging Reader (BioTek, Winooski, VT), equipped with a live cell module. Live cell images were then acquired at

2 hours intervals, using a 4 X phase-contrast objective, for a total of 12 hours for KP and KPK cells, or 18 hours for A549 cells. The cell image was captured and the average extent of wound closure was quantified by ImageJ software. Each experiment was performed in triplicate.

shRNA cloning and cell line generation

Doxycycline-induced knock down of *Bach1* and *Fbxo22* was achieved by cloning miR-E shRNAs targeting *Bach1* and *Fbxo22* into the LT3GEPIR vector as before (Sayin et al., 2017). Briefly, LT3GEPIR was digested with XhoI and EcoRI, and purified with a gel extraction kit (QIAGEN). Single stranded ultramers were amplified with forward primer miRE-XhoI (5' TGAACGCGAGAAGGTATATTGCT GTTACAGTGAGCG-3') and reverse primer miRE-EcoRI (5'-TCTCGAATTCTAGCCCCTTGAAGTCCGAGGCAGTAGGC-3'). Amplicons were gel purified, digested with XhoI and EcoRI, purified by PCR purification kit (QIAGEN) and ligated into the cut LT3GEPIR vector with T4 DNA Ligase at a 3:1 insert:vector molar ratio. Vectors were transduced into cells and selected with 3 and 6 $\mu\text{g/ml}$ puromycin for three plus three days. Knock down of mouse *Bach1/Bach1*, human *BACH1/BACH1*, mouse *Fbxo22/Fbxo22* and Human *FBXO22/FBXO22* was verified by western blot and qPCR analysis following 72 hr of treatment with 1 $\mu\text{g/ml}$ doxycycline. Cell lines transduced with the first two efficient shRNAs, along with a non-efficient shRNA as control, were used in the study (see Table S7). The LT3GEPIR vector was previously generated and described in detail (Fellmann et al., 2013). Sequences of ultramers obtained from Integrated DNA Technologies (Coralville, Iowa).

Tandem Mass Tag

The dried peptide mixture was re-suspended in 100 mM TEAB (pH 8.5) using a volume of 45 μL . Each sample was labeled with Tandem Mass Tag (TMT) reagent according to the manufacturer's protocol (Bhardwaj et al., 2017; Thompson et al., 2003). In brief, each TMT reagent vial (0.8 mg) was dissolved in 103 μL of anhydrous ethanol and was added to each sample. The reaction incubated for 60 min at room temperature and quenched using 8 μL of 5% w/v hydroxylamine. The samples were combined at a 1:1 ratio and the pooled sample was subsequently desalted using SCX and SAX solid-phase extraction columns (Strata, Phenomenex).

Offline fractionation of TMT multiplexed samples. The pooled sample was fractionated using basic pH reverse-phase HPLC as described (Bhardwaj et al., 2017). Briefly, the sample was loaded onto a 4.6 mm \times 250 mm Xbridge C18 column (Waters, 3.5 μm bead size) using an Agilent 1260 Infinity Bio-inert HPLC and separated over a 70 min linear gradient from 10 to 50% solvent B at a flow rate of 0.5 ml/min (Buffer A = 10 mM ammonium formate, pH 10.0; Buffer B = 90% ACN, 10 mM ammonium formate, pH 10.0). A total of 130 fractions were collected. The early, middle and late eluting fractions were concatenated and combined into 40 final fractions. The combined fractions were concentrated in the SpeedVac and stored at -80°C until further analysis.

Mass spectrometry analysis for multiplexed quantitation. An aliquot of each sample was loaded onto the same LC set up as described above. The peptide mixture was gradient eluted into the QExactive mass spectrometer (Thermo Scientific) using the following gradient: 5%–23% solvent B in 110 min, 23% –34% solvent B in 10 min, followed by 34%– 100% solvent B in 20 min. The full scan was acquired with a resolution of 70,000 (@ m/z 200), a target value of 1e6 and a maximum ion time of 120 ms. After each full scan 10 HCD MS/MS scans were acquired using the following parameters: resolution 35,000 (@ m/z 200), isolation window of 1.5 m/z , target value of 1e5, maximum ion time of 250 ms, normalized collision energy (NCE) of 30, and dynamic exclusion of 30 s.

Data analysis. The raw data was searched using MaxQuant (Cox and Mann, 2008) version 1.5.2.8. Proteins and peptides were searched against the UniProt mouse database using the Andromeda (Cox et al., 2011) search engine using a target-decoy approach and the following settings: two missed cleavages were allowed for trypsin; oxidation of methionine (M), and deamidation of asparagine (N) and glutamine (Q) were set as variable modifications; carbamidomethyl of cysteine (C) was set as fixed modifications; both precursor and fragment mass tolerances were set to 10 ppm; The peptide identifications were filtered using a false-discovery rate (FDR) of 0.01 at both the protein and peptide level. Only unique peptides were used for quantification and proteins identified with less than two unique peptides were excluded from analysis. The results were further filtered to remove common contaminant proteins and reverse identifications.

The bioinformatics analysis was performed using open source software Perseus (Version 1.6.0.2). The intensity values were log₂ transformed and missing values were imputed using the normal distribution as implemented by Perseus. A two-sided Welch's t test and Benjamini-Hochberg (Benjamini et al., 2001) FDR were performed. All expression levels, ratios and *p* values were reported, but only protein groups having an estimated FDR less than the cut-off level of 5% were considered significantly upregulated or downregulated.

Transcriptomics Data Analysis

Sequencing reads were mapped to the mouse reference genome (GRCm38.85/mm10) using the STAR aligner (v2.5.0c) (Dobin et al., 2013). Alignments were guided by a Gene Transfer Format file (Ensembl GTF version GRCh38.85). The mean read insert sizes and their standard deviations were calculated using Picard tools (v.1.126) (<http://broadinstitute.github.io/picard>). The read count tables were generated using HTSeq (v0.6.0) (Anders et al., 2015), normalized based on their library size factors using DESeq2 (Love et al., 2014), and differential expression analysis was performed with DESeq2 standard parameters (lfcshrink with apeglm estimation)(R version 3.5.2). DEGs with an absolute log₂ fold-change > 1 and False Discovery Rate (FDR) < 0.05 were identified as statistically significant. The FDR was calculated by applying Benjamini and Hochberg's method in the DESeq2 package. Each Ensembl (Zerbino et al., 2018) gene in the transcriptomic dataset was mapped to an MGI (Smith et al., 2018) mouse gene accession

using the mapping provided by Ensembl's biomaRt (Kinsella et al., 2011) such that each MGI mouse gene is represented by at most one Ensembl gene. This mapping was further leveraged to select a human ortholog from the orthology report downloaded from the Jackson Labs website (http://www.informatics.jax.org/downloads/reports/HGNC_homologene.rpt, downloaded on October 2018) such that every Ensembl gene maps to a single human ortholog. Many-to-one mappings between mouse and human genes were eliminated by selecting the candidate mouse gene with the maximal signal intensity across all samples. All downstream statistical analyses and generating plots were performed in R environment (v3.5.2) (<http://www.r-project.org/>).

Transwell Assays

Transwell assays for migration were performed in transwell inserts with a 6.5-mm, 8.0- μ m-pore polycarbonate membrane. Briefly, cells were suspended in serum-free media and seeded into the inner chamber (5×10^4 cells per chamber). The outer chamber contained complete growth media. Cells were incubated for 12 hours and then non-migrating cells on the inside of the membrane were carefully removed with a cotton swab, while migrating cells on the outside of the membrane were fixed, stained with 0.1% Crystal violet and photographed under a standard bright field microscope (10 X objective) equipped with a digital camera. At least 5 random fields/well were photographed and cells were counted for each field. Each experiment was performed in triplicate.

Volcano and Scatterplots

In Figures 4A and 4B, the volcano plots for each group comparison were generated by ggplot2 (3.0.0) package in R. In the plots in Figures 1G, 1H, and S1H the data points are colored by membership of any associated human ortholog (as described previously in the Transcriptomics Data Analysis section) in a comprehensive set of genes putatively regulated by Bach1 (integrated Bach1 gene set, described previously in the Gene Set Enrichment Analysis section). The shape of the data points indicates whether or not the human orthologs are members of HCMDB. When combining proteomics and transcriptomics data, individual data points are matched through their associated MGI accessions.

All the p -values associated with enrichment claims regarding significantly regulated genes (whether by transcriptomics or proteomics or both) result from one-sided Fisher Exact tests run in the R statistical language and environment (H. Wickham 2014). Differentially expressed genes/proteins all resulted from t tests on the underlying expression data (whether proteomic or transcriptomic) following a Benjamini-Hochberg procedure yielding a 5% False Discovery Rate. Biologically regulated genes were further filtered to include the requirement of an absolute \log_2 fold-change ≥ 1 .

QUANTIFICATION AND STATISTICAL ANALYSIS

All data were analyzed by Prism 7 (GraphPad). Statistical details of experiments can be found in the figure legends. Unless otherwise noted in figure legends, data are representative of at least three biologically independent experiments. Two-group datasets were analyzed by Student's unpaired t test. For three or more group analysis, one-way ANOVA multiple comparison test was used. The Kaplan-Meier log rank test was used for survival comparison. Fisher's exact test was used for calculating significance between groups in contingency tables, IHC, transcriptomic, proteomic and proteo-transcriptomic analyses. Extent of wound closure in scratch assay was quantified by ImageJ software 2.0. For all the statistical analysis: * = $p \leq 0.05$, ** = $p \leq 0.01$, *** = $p \leq 0.001$, **** = $p \leq 0.0001$.

DATA AND CODE AVAILABILITY

The original mass spectrometry data can be accessed through Mass Spectrometry Interactive Virtual environment (MassIVE) accession number MassIVE: MSV000083157 (<ftp://massive.ucsd.edu/MSV000083157>) and the ProteomeXchange Consortium accession number ProteomeXchange: PXD011818.

The original RNA sequencing data can be accessed through the GEO Repository at GEO: GSE122836.

Raw, uncropped supporting western blot files were deposited at Mendeley: <https://data.mendeley.com/datasets/m6vrdbwsnc/draft?a=42056e38-861b-41f1-a5c6-0fb9263327ff>

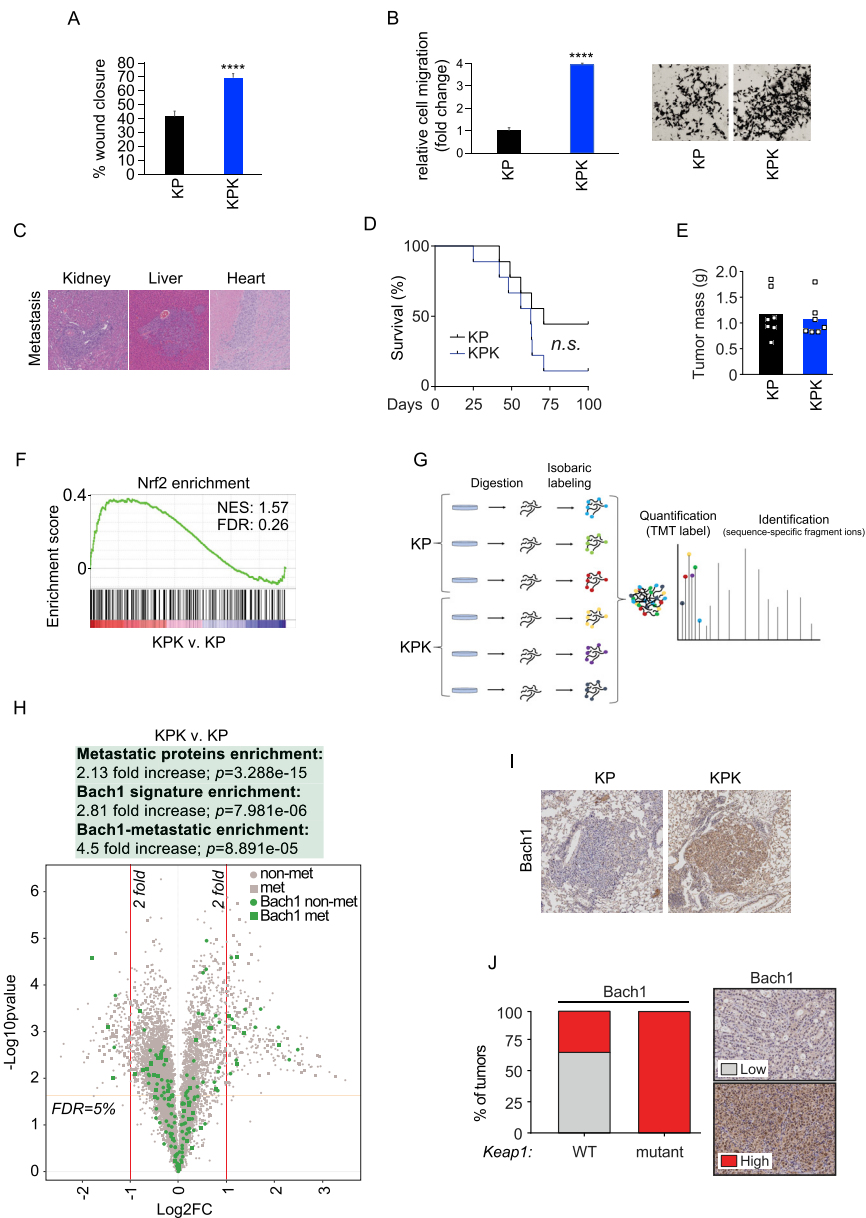


Figure S1. *Keap1* Loss Promotes Cell Migration, Metastasis, and Activation of the Bach1 Transcriptional Program, Related to Figure 1

(A) A scratch assay was performed over a 12 hours period using KP and KPK cells. The graph shows quantification of the wound closure from 3 technical replicates of a representative experiment. Values are presented as means \pm SEM.

(B) KP and KPK cells were tested for cell migration in a Boyden chamber assay over a 12 hours period. After this time, cells migrated to the bottom of the Transwells were fixed, stained, photographed, and counted in 5 different fields per well. The graph shows quantification from 3 technical replicates of a representative experiment. Right, representative images of migrated cells. Values are presented as means \pm SEM.

(C) Representative H&E images of distal metastasis from Figure 1B. Left, kidney metastasis; middle, liver metastasis; right, heart metastasis.

(D) Kaplan–Meier survival curves generated by comparing the mice used in the experiment shown in Figure 1B.

(E) Quantification of tumor masses obtained upon subcutaneous implantation of KPK or KP cells ($n = 7$ in each group) (see Figures 1C and 1D). Data are presented as means, and squares represent individual data points.

(F) Upregulation of Nrf2 transcriptional signature in sg*Keap1* cells compared to sg*Tom* cells.

(G) Experimental workflow of an isobaric multiplexed quantitative proteomics using Tandem Mass Tags to analyze the total proteome in KP and KPK cells as shown in (H).

(H) Volcano plot comparing the expression of HCMDDB proteins and Bach1 signature proteins between KPK and KP cells. Plotted for each protein are the negative log10 of the p value and the log2 of the fold change of protein expression of KPK cells relative to KP cells. The red bars represent fold change values of $-/+2$, and the yellow bar represents a FDR threshold of 5%. Circle data points represent non-metastatic proteins (non-met); square data points represent metastatic

(legend continued on next page)

proteins (met); gray data points represent non-Bach1 target proteins; green data points represent Bach1 target proteins. The enrichment of Metastatic proteins, Bach1 signature proteins, and Bach1-metastatic proteins was calculated by Fisher's exact test. FC, fold change.

(I) Representative IHC staining of Bach1 in distal metastases (related to [Figure 1A](#)). Scale bar 100 μ M.

(J) IHC analyses of Bach1 protein levels in LUAD PDXs carrying *Keap1* mutant ($n = 7$) v. LUAD PDXs carrying WT *Keap1* ($n = 11$). *Keap1* status (WT or mutant) was confirmed in all tumor samples by targeted exome sequencing. Right, representative IHCs with low or high levels of Bach1. Bach1 levels increase in mutant-*Keap1* versus WT *Keap1* biopsies: $p = 0.0128$. Scale bar 100 μ M.

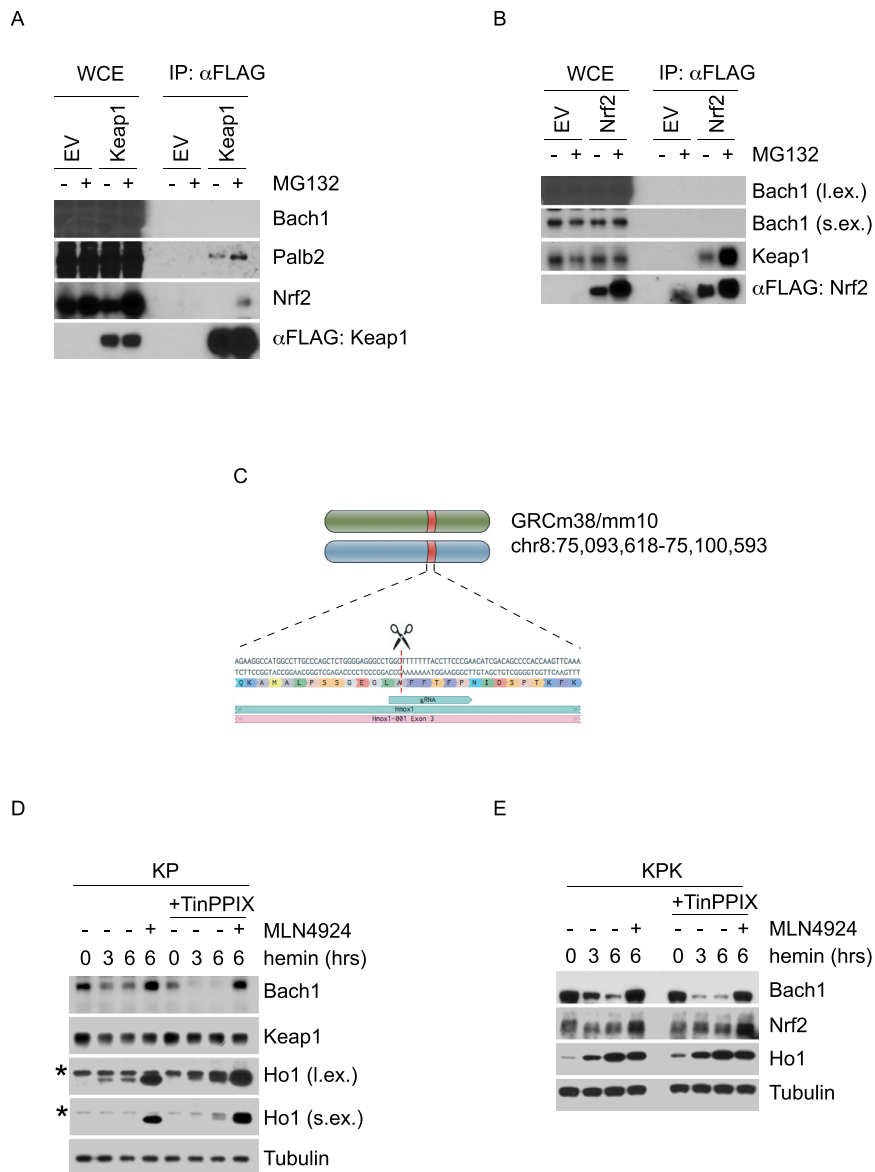


Figure S2. Keap1 Loss Promotes Bach1 Accumulation through Nrf2-Dependent Induction of Ho1, Related to Figure 2

(A) HEK293T cells were transfected with either an empty vector (EV) or FLAG-tagged Keap1. Twenty-four hours post-transfection, cells were treated with MG132 for 3 hours and then collected for immunoprecipitation (IP) and immunoblotting. WCE, whole-cell extract.

(B) HEK293T cells were transfected with either an EV or FLAG-tagged Nrf2. Twenty-four hours post-transfection, cells were treated with MG132 for 3 hours, and then collected for immunoprecipitation (IP) and immunoblotting. WCE, whole-cell extract. l.ex., long exposure; s.ex., short exposure.

(C) Schematic representation of the *Hmox1* genomic locus and gRNA target location. Exon 1 refers to the mouse *Hmox1* gene (GRCm38/mm10; chr8:75,093,618-75,100,593).

(D) KP cells were treated with hemin (10 μ M), collected at the indicated times, lysed, and immunoblotted as indicated. Before hemin treatment, cells were pretreated for 30 minutes with TinPPIX (10 μ M) in the presence or absence of MLN4924 (2 μ M) as indicated. The * denotes a nonspecific band. l.ex., long exposure; s.ex., short exposure.

(E) KPK cells were treated with hemin (10 μ M), collected at the indicated times, lysed, and immunoblotted as indicated. Before hemin treatment, cells were pretreated for 30 minutes with TinPPIX (10 μ M) in the presence or absence of MLN4924 (2 μ M) as indicated.

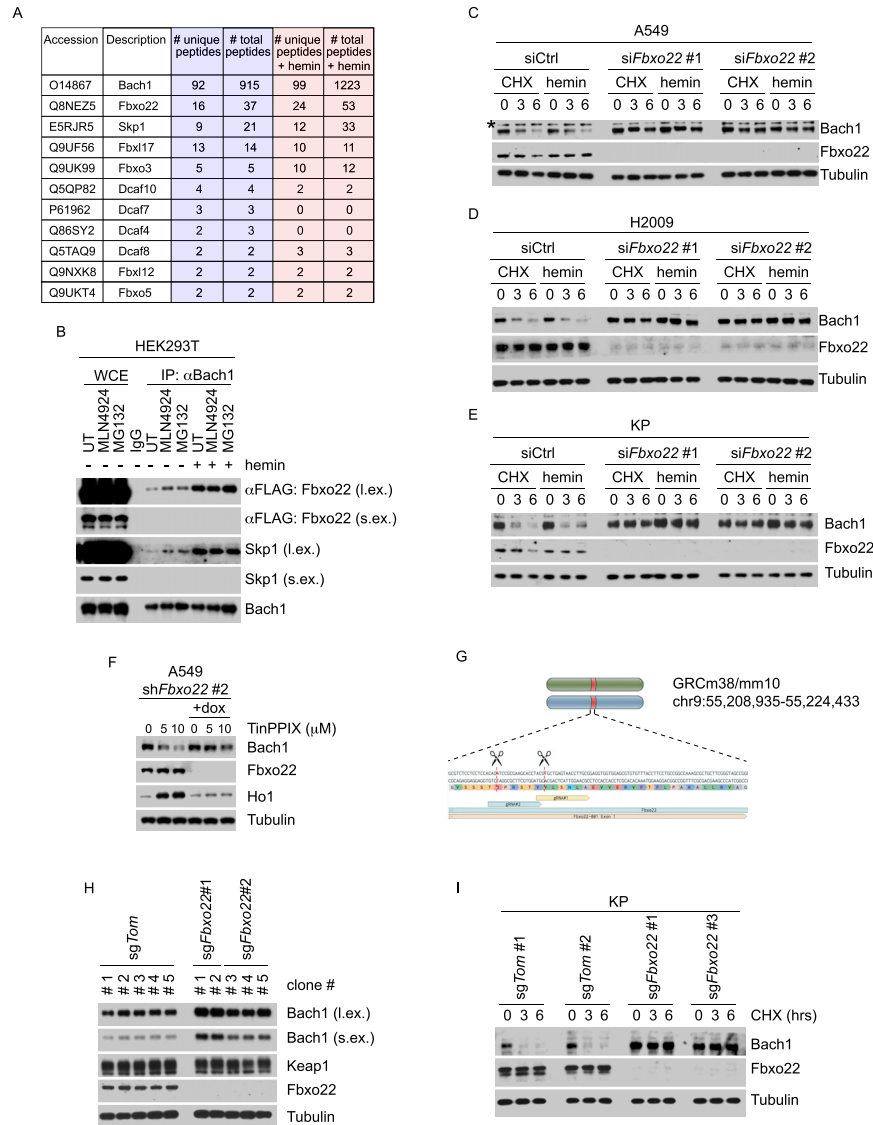


Figure S3. Fbxo22 Mediates the Heme-Induced Degradation of Bach1, Related to Figure 3

(A) FLAG-tagged human Bach1 was immunoprecipitated from HEK293T cells and subjected to mass spectrometry analysis. Where indicated, before harvesting, cells were treated for 1 hour with hemin (10 μM). The table lists the number of unique and total peptides for each Bach1 interacting protein that is a subunit of an ubiquitin ligase complex.

(B) HEK293T cells were transfected with FLAG-tagged Fbxo22. Twenty-four hours post-transfection, cells were treated with either MG132 or MLN4924 for 3 hours, collected for immunoprecipitation (IP) with either nonspecific IgG or an antibody against Bach1, treated with hemin (10 μM) where indicated, and immunoblotted as indicated. l.ex., long exposure; s.ex., short exposure.

(C) A549 cells were transfected for 24 hours with either a non-targeting siRNA (siCtrl) or 2 different siRNA oligos targeting *Fbxo22* (siFbxo22). Cells were then treated with either cycloheximide (CHX) or hemin, collected at the indicated times, lysed and immunoblotted as indicated. The * denotes a nonspecific band.

(D) H2009 cells were transfected for 24 hours with either siCtrl or 2 different siFbxo22. Cells were then treated with either CHX or hemin, collected at the indicated times, lysed and immunoblotted as indicated.

(E) KP cells were transfected for 24 hours with either siCtrl or 2 different siFbxo22. Cells were then treated with either CHX or hemin, collected at the indicated times, lysed and immunoblotted as indicated.

(F) A549 cells infected with lentiviruses expressing an shRNA targeting *Fbxo22* (shFbxo22) under the control of a doxycycline-inducible promoter were treated (where indicated) with doxycycline for 24 hours. Cells were then treated with TinPPIX at the indicated concentrations for 24 hours, lysed and immunoblotted as indicated.

(G) Schematic representation of the *Fbxo22* genomic locus and 2 different gRNA target locations. Exon 1 refers to the mouse *Fbxo22* gene (GRCm38/mm10; chr9:55,208,935-55,224,433).

(H) The indicated proteins in KP-sgTom and KP-sgFbxo22 clones were analyzed by immunoblot. l.ex., long exposure; s.ex., short exposure.

(I) Two different KP-sgTom and 2 different KP-sgFbxo22 clones were treated with CHX, collected at the indicated times, lysed, and immunoblotted as indicated.

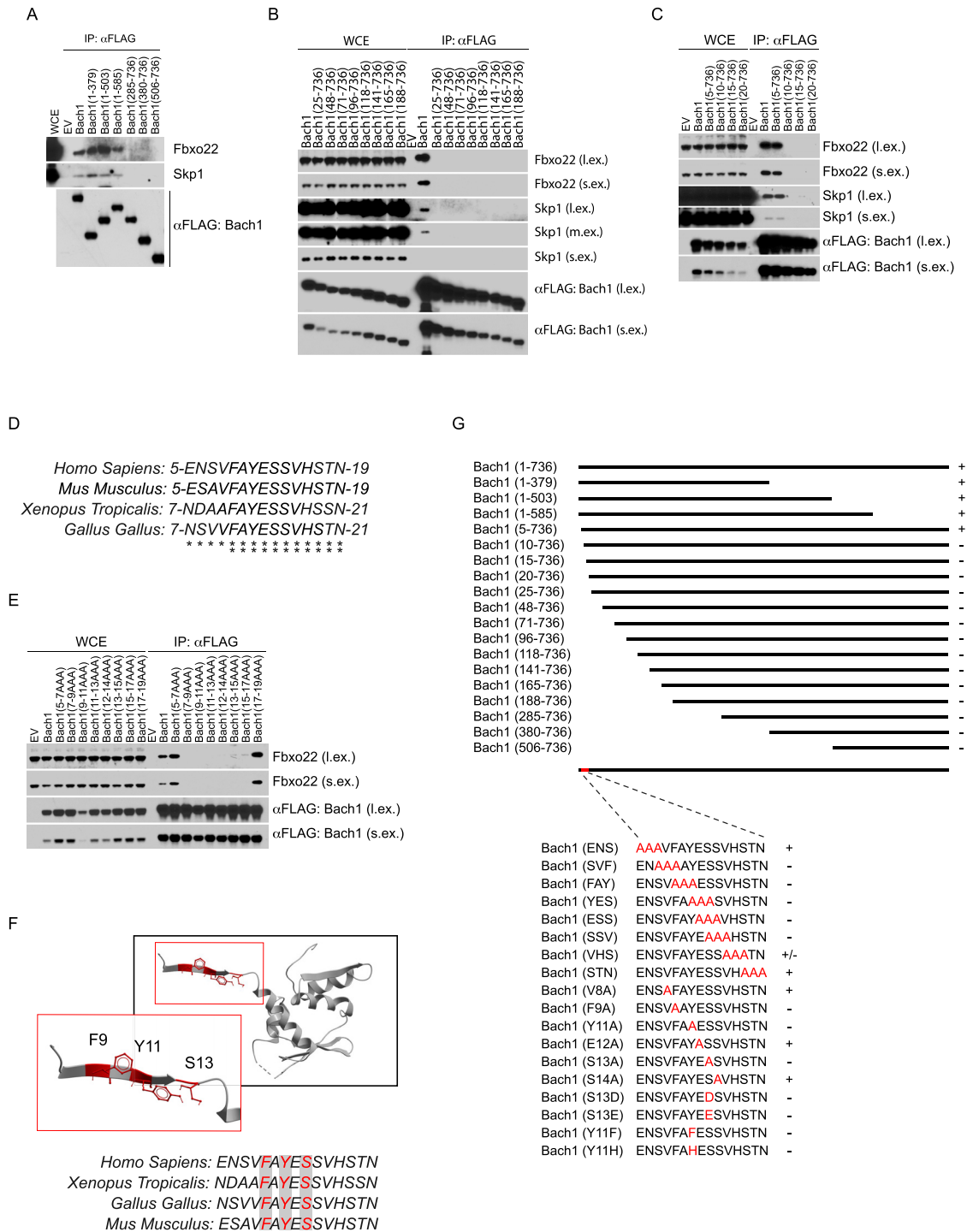


Figure S4. Mapping of the Fbxo22 Degron in Bach1, Related to Figure 3

(A) HEK293T cells were transfected with either an EV or the indicated FLAG-tagged proteins (i.e., wild-type Bach1 or Bach1 mutants). Twenty-four hours post-transfection, cells were treated with MLN4924 for 3 hours before collection for immunoprecipitation (IP) and immunoblotting as indicated. WCE, whole-cell extract.

(B) The experiment was performed as described in (A), except that different Bach1 mutants were used. l.ex., long exposure; m.ex., medium exposure; s.ex., short exposure.

(C) The experiment was performed as described in (A), except that different Bach1 mutants were used. l.ex., long exposure; s.ex., short exposure.

(legend continued on next page)

(D) Alignment of the Bach1 aminoacidic sequence mediating the binding to Fbxo22 (amino acids 5 - 19 of human Bach1), across different Bach1 orthologs. Conserved residues are marked by two * and analog residues by one *.

(E) The experiment was performed as described in (A), except that different Bach1 mutants were used. WCE, whole-cell extract. l.ex., long exposure; s.ex., short exposure.

(F) Top, 3D structure of Bach1 BTB domain (PDB: 2IHC). 3D structure image was generated with ICM 3.8-4a (Molsoft LLC, La Jolla, CA). The 3 critical amino acids (F9, Y11 and S13) required for binding to Fbxo22 are highlighted in red. Bottom, the alignment of the aminoacidic sequence (degron motif) required for binding to Fbxo22, across Bach1 orthologs. The 3 critical amino acids (F9, Y11 and S13) required for binding to Fbxo22 are highlighted in red.

(G) Schematic representation of Bach1 mutants used in mapping experiments. The Bach1 mutants found to interact with Fbxo22 are indicated by the symbol "+," "+/-" denotes reduced binding, and "-" denotes undetectable binding.

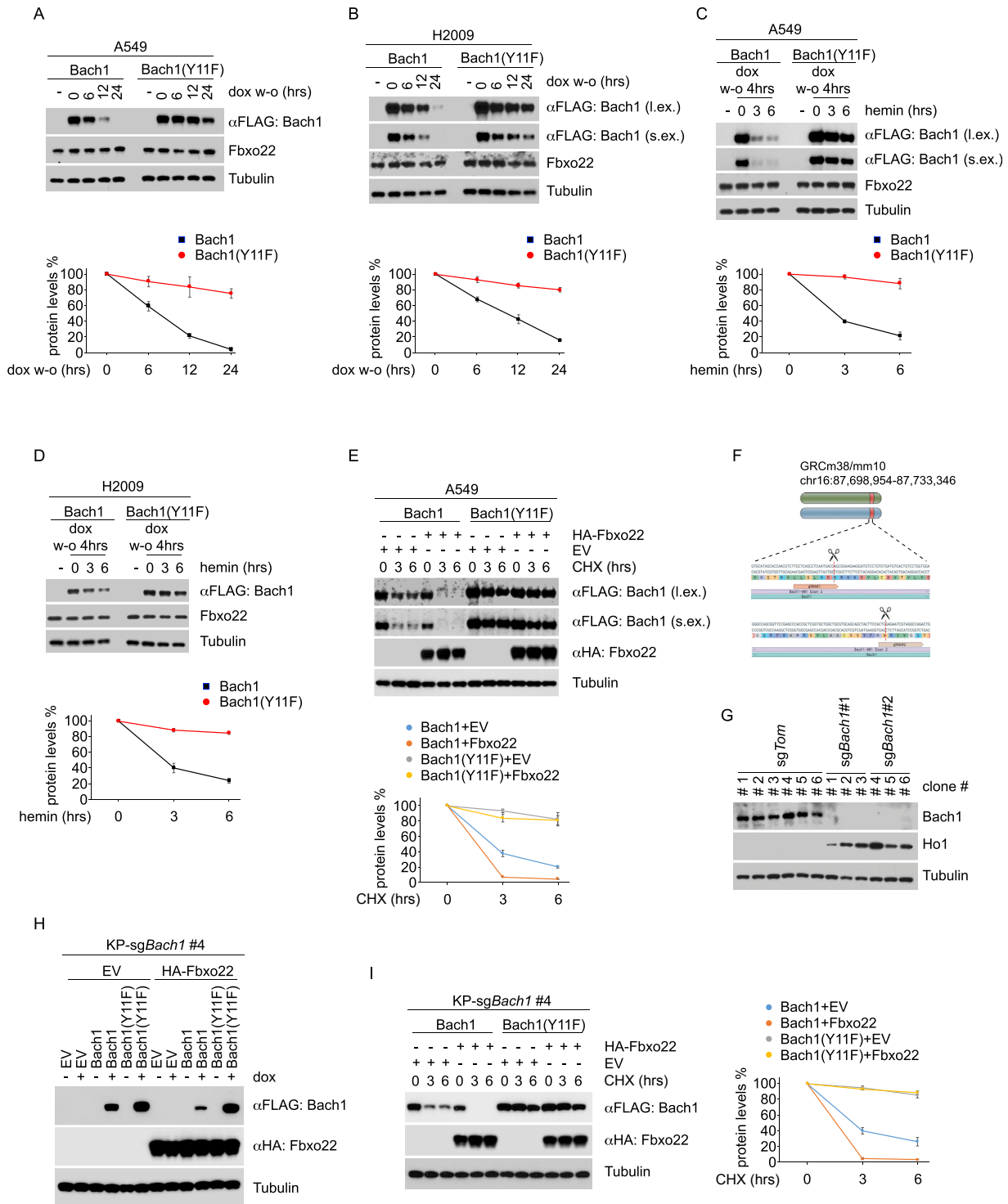


Figure S5. Fbxo22 Mediates the Heme-Induced Degradation of Bach1, Related to Figure 3

(A) A549 cells infected with lentiviruses expressing either FLAG-tagged WT Bach1 or Bach1(Y11F) under the control of a doxycycline-inducible promoter were treated (where indicated) with doxycycline for 24 hours. Doxycycline was then washed out to stop transcription and allow protein decay, and cells were collected at the indicated times, lysed, and immunoblotted as indicated. The graph shows the quantification of protein levels. Values are presented as means \pm SEM. w-o, wash-out.

(B) H2009 cells infected with lentiviruses expressing either FLAG-tagged WT Bach1 or Bach1(Y11F) under the control of a doxycycline-inducible promoter were treated (where indicated) with doxycycline for 24 hours. Doxycycline was then washed out to stop transcription and allow protein decay, and cells were collected

(legend continued on next page)

at the indicated times, lysed, and immunoblotted as indicated. The graph shows the quantification of protein levels. Values are presented as means \pm SEM. l.ex., long exposure; s.ex., short exposure; w-o, wash-out.

(C) A549 cells infected with lentiviruses expressing either FLAG-tagged WT Bach1 or Bach1(Y11F) under the control of a doxycycline-inducible promoter were treated (where indicated) with doxycycline for 24 hours. Doxycycline was then washed out and, after 4 hours, cells were treated with hemin (10 μ M), collected at the indicated times, lysed, and immunoblotted as indicated. The graph shows the quantification of protein levels. Values are presented as means \pm SEM. l.ex., long exposure; s.ex., short exposure; w-o, wash-out.

(D) H2009 cells infected with lentiviruses expressing either FLAG-tagged WT Bach1 or Bach1(Y11F) under the control of a doxycycline-inducible promoter were treated (where indicated) with doxycycline for 24 hours. Doxycycline was then washed out and, after 4 hours, cells were treated with hemin (10 μ M), collected at the indicated times, lysed, and immunoblotted as indicated. The graph shows the quantification of protein levels. Values are presented as means \pm SEM. w-o, wash-out.

(E) A549 cells infected with lentiviruses expressing either FLAG-tagged WT Bach1 or Bach1(Y11F) under the control of a doxycycline-inducible promoter were transfected with either an EV or HA-tagged Fbxo22 as indicated. Cells were treated with doxycycline for 24 hours. Doxycycline was then washed out and, after 4 hours, cells were treated with CHX, collected at the indicated times, lysed, and immunoblotted as indicated. The graph shows the quantification of protein levels. Values are presented as means \pm SEM. l.ex., long exposure; s.ex., short exposure.

(F) Schematic representation of the *Bach1* genomic locus and 2 different gRNA target locations. Exon 2 refers to the mouse *Bach1* gene ([GRCm38/mm10; chr16:87,698,954-87,733,346](#)).

(G) The indicated proteins in KP-sg*Tom* and KP-sg*Bach1* clones were analyzed by immunoblot.

(H) KP-sg*Bach1* clone #4 was infected with lentiviruses expressing either an EV, FLAG-tagged WT Bach1, or Bach1(Y11F) under the control of a doxycycline-inducible promoter in combination with lentiviruses expressing either an EV or HA-tagged Fbxo22. Where indicated, cells were treated with doxycycline for 24 hours. Protein expression was analyzed by immunoblot with antibodies to the indicated proteins.

(I) Cells used in (H) were treated with doxycycline for 24 hours. Doxycycline was then washed out and, after 4 hours, cells were treated with CHX, collected at the indicated times, lysed, and immunoblotted as indicated. The graph shows the quantification of protein levels. Values are presented as means \pm SEM.

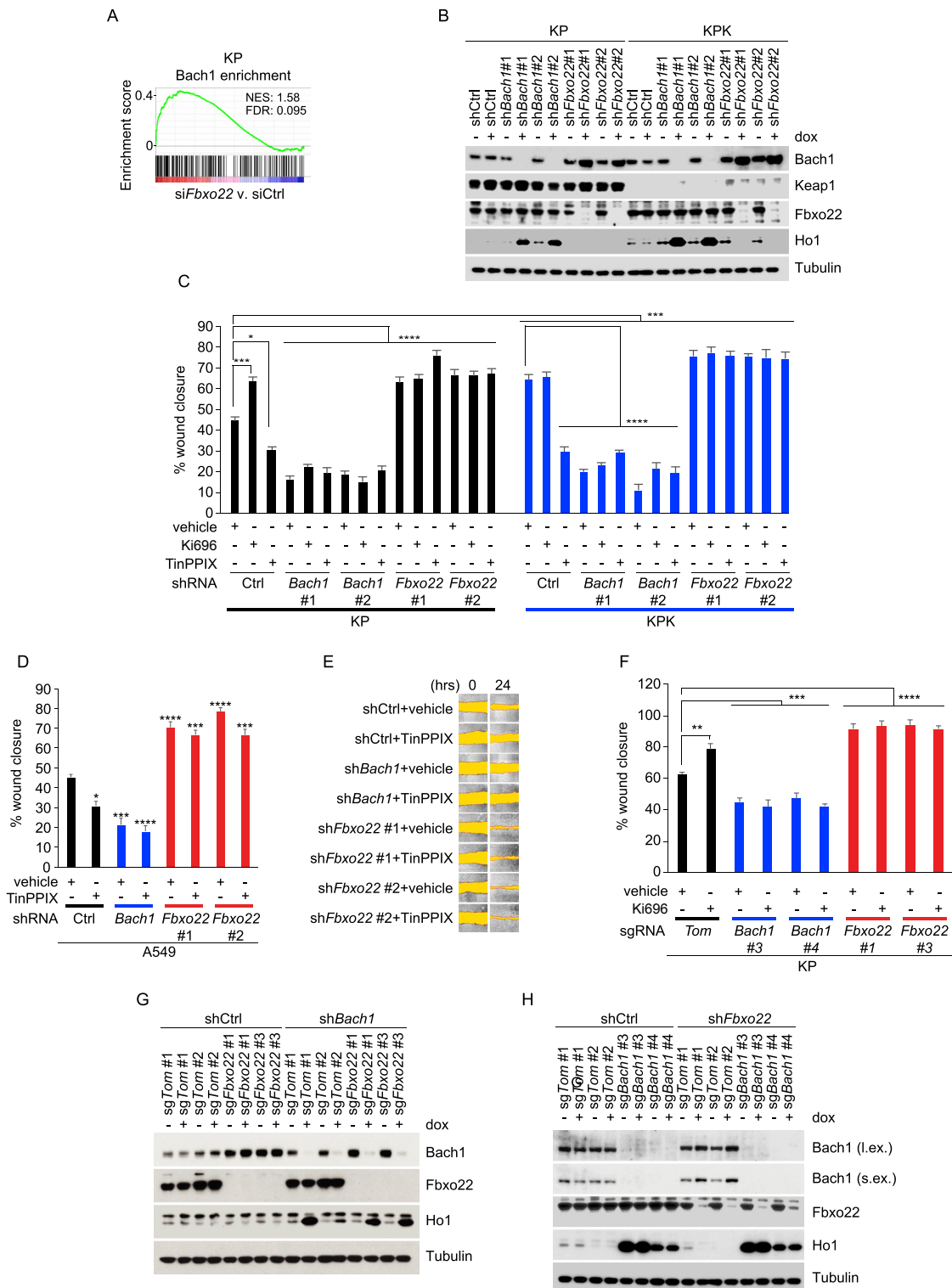


Figure S6. Bach1 Levels Regulate Cell Migration, Related to Figure 4

(A) Upregulation of Bach1 transcriptional signature in KP cells transfected with *siFbxo22* compared to KP cells transfected with *siCtrl*.
 (B) KP and KPK cells infected with lentiviruses expressing either a doxycycline-inducible non-targeting shRNA (*shCtrl*), 2 different shRNA targeting *Bach1* (*shBach1*) or 2 different shRNA targeting *Fbxo22* (*shFbxo22*) were treated with doxycycline for 48 hours (where indicated). Cells were then collected, lysed, and immunoblotted as indicated.

(legend continued on next page)

(C) KP and KPK cells generated as in (B) were treated with doxycycline for 48 hours. Cells were then treated with either vehicle, Ki696 (1 μ M) or TinPPIX (10 μ M) as indicated. After 24 hours, a scratch assay was performed over a 12 hours period. The graph shows quantification of the wound closure from 3 technical replicates of a representative experiment. Values are presented as means \pm SEM.

(D) A549 cells infected with lentiviruses expressing either shCtrl, sh*Bach1* or 2 different sh*Fbxo22* under the control of a doxycycline-inducible promoter were treated with doxycycline for 48 hours. Cells were then treated with either vehicle or TinPPIX (10 μ M) as indicated. After 24 hours, a scratch assay was performed over a 18 hours period. The graph shows quantification of the wound closure from 3 technical replicates of a representative experiment. Values are presented as means \pm SEM. * indicate statistical significance obtained from comparing samples to the shCtrl untreated sample.

(E) Representative images of wound closure from the experiments quantified in (D).

(F) KP-sg*Tom*, 2 different KP-sg*Bach1* clones (see [Figure S5G](#)), and 2 different KP-sg*Fbxo22* clones (see [Figure S3H](#)) were treated with either vehicle or Ki696 (1 μ M) as indicated. After 24 hours, a scratch assay was performed over a 12 hours period. The graph shows quantification of the wound closure from 3 technical replicates of a representative experiment. Values are presented as means \pm SD.

(G) Two different KP-sg*Tom* and 2 different KP-sg*Fbxo22* clones (see [Figure S3H](#)) were infected with lentiviruses expressing either shCtrl or sh*Bach1* under the control of a doxycycline-inducible promoter. Where indicated, cells were treated with doxycycline for 48 hours. Cells were then collected, lysed, and immunoblotted as indicated.

(H) Two different KP-sg*Tom* and 2 different KP-sg*Bach1* clones (see [Figure S5G](#)) were infected with lentiviruses expressing either shCtrl or sh*Fbxo22* under the control of a doxycycline-inducible promoter. Where indicated, cells were treated with doxycycline for 48 hours. Cells were then collected, lysed, and immunoblotted as indicated.

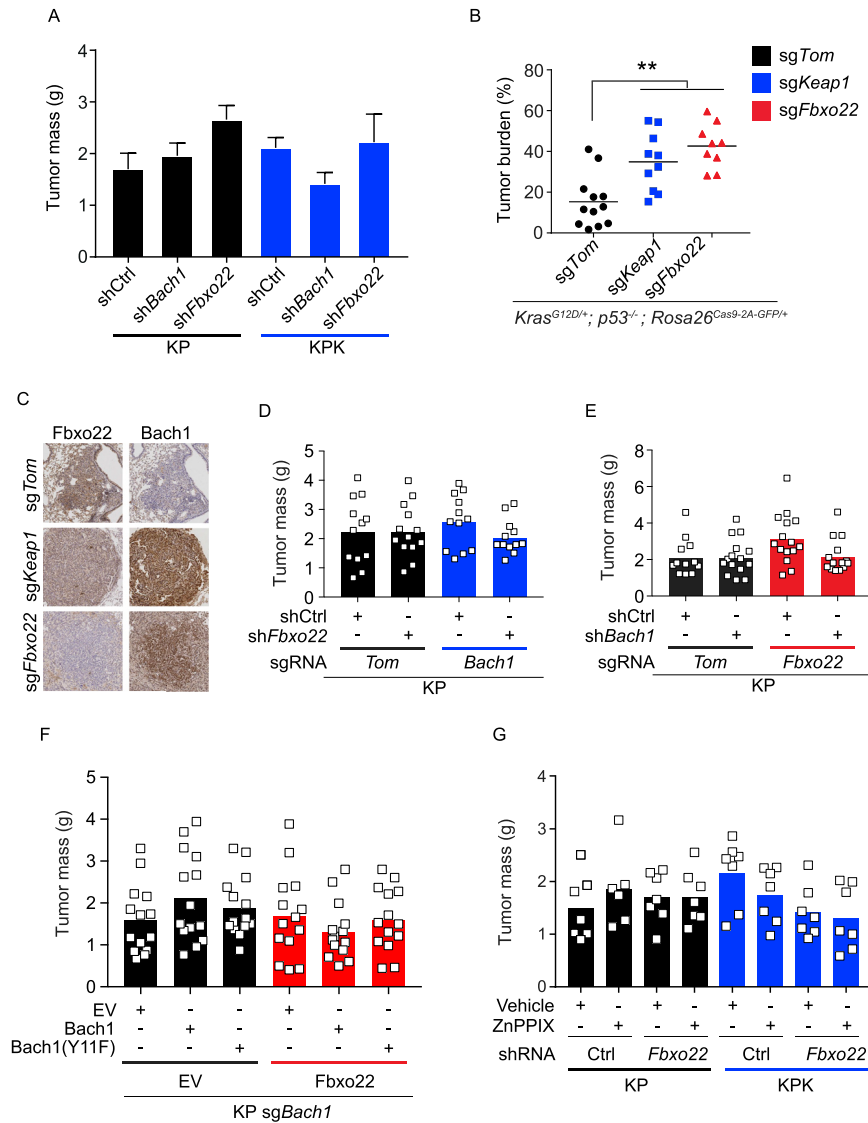


Figure S7. Bach1 Promotes Metastasis, Related to Figures 5 and 6

(A) Quantification of tumor masses obtained upon subcutaneous implantation of various KPK or KP cells described in the legend of Figure 5A. Values are presented as means \pm SEM.

(B) Quantification of tumor burden (total tumor area/total lung area) in mice used for the experiment shown in Figure 5C. Data are presented as means, and symbols represent individual data points.

(C) Representative IHC staining of Bach1 and Fbxo22 in primary tumors from sgTom, sgKeap1, and sgFbxo22 mice used for the experiment shown in Figure 5C. Scale bar 100 μ M.

(D) Quantification of tumor masses obtained upon subcutaneous implantation of various KP cells described in the legend of Figure 5D. Data are presented as means, and squares represent individual data points.

(E) Quantification of tumor masses obtained upon subcutaneous implantation of various KP cells described in the legend of Figure 5E. Data are presented as means, and squares represent individual data points.

(F) Quantification of tumor masses obtained upon subcutaneous implantation of various KP cells described in the legend of Figure 6A. Data are presented as means, and squares represent individual data points.

(G) Quantification of tumor masses obtained upon subcutaneous implantation of various KPK or KP cells described in the legend of Figure 6B. Data are presented as means, and squares represent individual data points.